Fe Coordination Environment, Fe-Incorporated Ni(OH)₂ Phase, and Metallic Core are Key Structural Components to Active and Stable Nanoparticle Catalysts for the Oxygen Evolution Reaction

Prashant Acharya,^a Ryan H. Manso,^b Adam S. Hoffman,^c Sergio I. Perez Bakovic,^a László Kékedy-Nagy,^{a,d} Simon R. Bare,^c Jingyi Chen,^b Lauren F. Greenlee^{a,e,*}

^aRalph E. Martin Department of Chemical Engineering, University of Arkansas, Fayetteville, AR, USA 72701

^bDepartment of Chemistry & Biochemistry, University of Arkansas, Fayetteville, AR, USA 72701

^cStanford Synchrotron Radiation Lightsource, Menlo Park, CA, USA 94025

^dDepartment of Electrical and Computer Engineering, Concordia University, Montreal, QC, H3G 1M8, Canada

^eDepartment of Chemical Engineering, Pennsylvania State University, University Park, PA, USA 16802

*Corresponding Author email: greenlee@psu.edu

1. Abstract

Bimetallic iron-nickel oxide/hydroxide (FeNiO(H)_x) nanocatalysts have emerged as non-precious metal candidates for alkaline oxygen evolution reaction (OER) electrocatalysis. However, there are still significant open questions regarding the role of electrocatalyst synthesis route, and the resulting electrocatalyst morphology and nanoscale structure, in determining the operando atomic scale structure when subjected to the Faradaic OER voltage environment. Herein, we report on two nanoparticle FeNiO(H)_x electrocatalysts and their differing chemical structure using operando x-ray absorption spectroscopy (XAS) studies at relevant OER conditions. The two bimetallic nanoparticle electrocatalysts were synthesized using aqueous (NP-aq) vs. oil-based (NP-oil) synthesis routes but resulted in compositionally similar surface chemistry as-synthesized. Operando XAS results suggest Ni oxidizes from the initial +2 oxidation state to +3/+4 state reminiscent of the transformation of α -Ni(OH)₂ to γ -NiOOH; the oxidation state change is voltage dependent and occurs in both NP-aq and NP-oil nanoparticles. There does not appear to be an oxidation state change for Fe, but Fe coordination environment does change with voltage. The NPaq nanoparticles resulted in Fe coordination transitions between Fe^{3+} T_d , observed in assynthesized and 0.8 - 0.9 V vs. Ag/AgCl conditions, and Fe³⁺ O_h , observed at 0 V vs. Ag/AgCl, while the NP-oil nanoparticles resulted in a largely stable Fe³⁺ O_h coordination with more subtle changes in coordination environment. The voltage dependence of this Fe coordination transition is nanoparticle-dependent, with NP-aq nanoparticles transitioning dramatically at 0.7 V vs. Ag/AgCl, but NP-oil nanoparticles transitioning slowly starting at 0.1 V vs. Ag/AgCl. Additionally, a shortening of both the Fe-O and Ni-O bond distances occurs for both nanoparticle materials, but the magnitude of change is different for NP-aq versus NP-oil, suggesting the nanoparticle structures result in unique changes under applied potential. EXAFS analysis showed distinct chemical environments for the Fe species of NP-aq vs. NP-oil, metallic Fe and Ni character in NP-aq, and Ni largely in a hydroxide phase for both nanoparticles. NP-aq results in improved activity and stability during OER, as compared to NP-oil, suggesting that the Fe³⁺ $O_h \rightarrow T_d$ transition, metallic core, and a predominant Fe-incorporated Ni(OH)₂ phase in the shell are important for OER performance. This study highlights that both the electrochemical environment and the as-synthesized morphology of nanoparticle electrocatalysts are important in determining the operational chemical structures and structure-performance relationships.

Keywords: Alkaline oxygen evolution reaction; iron-nickel oxide; nanoparticle; electrocatalyst; operando x-ray absorption spectroscopy

2. Introduction

Transition metal based oxides and hydroxides have been extensively studied as oxygen evolution reaction (OER) catalysts in the last decade as they have been shown to considerably improve the sluggish OER kinetics in alkaline systems.¹⁻⁴ Among them, the iron-nickel bimetallic oxide/hydroxide materials have been of particular interest as they are predicted theoretically⁵⁻⁶ and demonstrated experimentally⁷⁻⁸ to result in low OER overpotentials and enhanced kinetics. With the confirmation that the iron component is necessary for FeNiO(H)_x OER activity, ^{7, 9-10} we seek to understand the role(s) that nanoparticle synthesis and the presence of iron species play in OER enhancement of nickel oxide and hydroxide electrocatalysts through atomic scale structural characterization. Synchrotron-based x-ray absorption spectroscopy (XAS) has developed a current picture of as-synthesized FeNiO(H)_x films, where Fe species appear to incorporate into α -Ni(OH)₂, substituting for Ni within the hydroxide crystal structure and occupying an octahedral coordination environment.¹¹ The structure of synthesized nanoparticle catalysts is more diverse, ranging from cubic Fe-substituted NiO¹²⁻¹⁴ and nickel ferrite spinel (NiFe₂O₄)^{12, 15} to NiFe layered double hydroxides, 16-17 amorphous nanoscale Fe-doped LaNiO₃, 18 Fe-doped Ni(OH)₂, 19-20 physical mixtures of Ni(OH)₂ and FeOOH,²¹ FeNiO_x nanofiber structures,²² hollow nanoparticles and nanotubes, 23-24 and core-shell FeNiO_x structures, 25-26 among others. Our prior work 20, 25 on two synthesis routes (low-temperature aqueous phase and high temperature organic phase) to obtain FeNiO_x nanoparticles suggested similar disordered Ni(OH)₂-like structure with iron incorporation, and similar oxide/hydroxide surface chemistry, but differences in morphology. Connections between as-synthesized and operando chemical structure of these FeNiO_x electrocatalysts remain limited, with operando studies primarily focused on films. In the present study, we focus on analyzing similarities and differences in operando atomic structure between the two nanoparticle

catalysts, with the goal of understanding how as-synthesized structure and synthesis route can affect the iron and nickel chemistry during the OER.

Operando XAS studies of (Fe)Ni(OH)₂ films have revealed that metal-oxygen bond length compression occurs in both the Fe-O and Ni-O atomic pairs under applied voltages within the OER Faradaic regime, 11, 27 with mirrored compressions of the metal-metal atomic pairs in the second coordination shell. Friebel et al. 11 also reported a decrease in the coordination number for Fe in Fe₂₅Ni₇₅OOH from 6.5 to 5.4 under applied voltage, while the predicted coordination number for Ni in the same electrocatalyst film changes more subtly from 6.5 to 6.1. Both metals were modeled to be in octahedral coordination environments, with the lowest theoretically-predicted OER overpotential to be the same for either an Fe on-top site of Fe-doped γ-NiOOH or a Fe-Fe bridge site of Ni-doped γ-FeOOH.¹¹ The shape and absorption energy of the pre-edge feature in the Fe K-edge XAS spectra reported by Friebel et al. 11 show little change as a function of applied voltage, suggesting that the majority of the Fe species in (Fe)Ni(OH)₂ films does in fact remain in a similar coordination environment throughout the voltage window tested. However, Friebel et al.¹¹ suggested that a small fraction (~10%) of the Fe species may exist in tetrahedral coordination under OER conditions. The uncertainty of this result (i.e., the unknown fraction of possible Fe T_d species) hints at some of the complexity of the (Fe)Ni(OH)₂ film catalysts.

It has also been suggested that Fe can also incorporate into edge or defect sites of Ni(OH)₂-type materials, 28 and that the resulting Fe-doped NiOOH structures are in fact responsible for enhanced OER activity, rather than bulk Fe-substituted Ni(OH)₂. These structures are likely to contain undercoordinated octahedral Fe³⁺ species, or even tetrahedral coordination sites, as was recently suggested by Song et al., 29 for surface-associated γ -FeOOH on γ -NiOOH. Confounding results have also been reported, where operando XAS^{12, 17} or quasi-operando (i.e., freeze quenched)

XAS³⁰⁻³¹ studies have revealed little to no change in the Fe and/or Ni K-edge spectra. Further complications arise from interpreting the studies of both Gorlin et al.³⁰⁻³¹ and Abbott et al.¹² because FeNiO_x nanoparticulate materials were investigated rather than films^{11, 27} or micrometerscale particles.¹⁷ However, both studies suffer from experimental limitations that confound any possible conclusion about nanoparticle vs. film morphology. The work of Gorlin et al.³¹ used a "quasi in situ" XAS approach, where catalysts were freeze quenched post-electrochemistry and stored in liquid N₂ for XAS analysis; this approach is actually a post-mortem characterization method and means that the catalysts were not under applied potential during XAS measurement and therefore were not true operando studies. Abbott et al. 12 conducted true operando XAS experiments, but only evaluated up to a voltage of 1.65 V vs. RHE; our results in the present study suggest that significant structural change occurs above this voltage and suggest that the study by Abbott et al.¹² did not evaluate high enough voltages to observe the structural changes that we report herein. As a result, erroneous conclusions may be made about nanoparticle vs. film morphologies based on these two papers. Few operando XAS studies beyond that of Friebel et al. 11 have reported detailed regions of the Fe pre-edge feature of Fe K-edge spectra, even though Fe coordination environment, oxidation state, and orbital mixing can be assessed both qualitatively and quantitatively via Fe K-edge pre-edge analysis. 32-37

Thus, open questions remain around the role(s) of electrocatalyst morphology, nanoscale structure, electrocatalyst synthesis route, and the route of Fe incorporation in determining the operando atomic scale structure that exists in $FeNiO(H)_x$ electrocatalysts when subjected to the Faradaic OER voltage environment. These questions include if and how electrocatalyst morphology and synthesis route impact operando chemical structure and OER performance. Further, there remains an open debate around the active site structure(s) for $FeNiO(H)_x$ -type OER electrocatalysts, where

both detailed operando XAS studies and theoretical efforts must advance simultaneously and iteratively to fully describe the dynamic electronic and chemical structures of both Fe and Ni in these complex materials. The debate around active structure includes how the Fe electronic structure changes under OER voltages and whether the Ni species shifts to a higher oxidation state in all FeNiO(H)_x morphologies (i.e., both films and nanoparticles). Unfortunately, both the Gorlin et al.³¹ and Abbott et al.¹² XAS studies on nanoparticles do not allow conclusions on nanoparticles vs. films due to the experimental limitations described above. This debate thus needs to be resolved, particularly for nanoparticulate FeNiO(H)_x materials, to understand the details of FeNiO(H)_x active site structure and the role(s) of synthesis route and as-synthesized structure on OER performance metrics. In particular, the Fe atomic scale coordination environment needs to be better understood, and Fe and Ni atomic scale chemistries must be probed more in detail for nanostructured materials.

In this work, we compare two different FeNiO(H)_x nanocatalysts that were synthesized via either aqueous-phase solution synthesis or organic-phase solution synthesis. Our previous work has characterized these nanoparticle electrocatalysts for OER performance and in detail with ex situ characterization techniques.^{20, 25, 38-39} The two synthesis routes produce a nominal Fe₂₀Ni₈₀ ratio in a bimetallic alloy core-bimetallic oxide shell nanoparticle (aqueous phase synthesis, from here on referred to as NP-aq) and a NiO_x core-NiO_x/FeO_x shell nanoparticle (organic solution synthesis, from here on referred to as NP-oil). The organic-phase approach produces nanoparticles with a highly uniform size and shape and a well-defined core-shell morphology. In contrast, the aqueous-phase approach yields a nanoparticle morphology with significantly less uniform size and coreshell structure, where both nanoparticle materials resulted in a disordered oxide/hydroxide phase, with iron-incorporated nickel hydroxide at the as-synthesized surface. With a similar as-

synthesized oxide/hydroxide surface chemistry having a disordered α -Ni(OH)₂-associated phase, ^{20, 25} we used these two nanoparticle OER electrocatalysts to compare and contrast Fe and Ni atomic scale structure as a function of applied voltage with operando XAS. Even though XAS is a bulk characterization technique, we assume that the changes observed under operando conditions reflect the chemistry of electrochemically accessible species. We probe both the x-ray absorption near edge structure (XANES) and the extended x-ray absorption fine structure (EXAFS) regions of the Fe K-edge and the Ni K-edge and perform an analysis of the pre-edge regions for both absorption edges. In addition, we model the EXAFS regions of both edges based on a γ -FeOOH base crystal structure¹¹ to understand how the coordination environment changes as a function of voltage. Overall, we observe significant changes in both Fe and Ni atomic-scale structure as a function of both nanoparticle type and voltage conditions, suggesting that both the electrochemical environment and the as-synthesized morphology of these nanoparticle electrocatalysts are important in determining the operational chemical structure of the OER catalyst.

3. Experimental Section

3.1 Materials

Chemicals were obtained as ACS grade commercial products and used without further purification unless specified. Iron(II) sulfate heptahydrate (FeSO₄.7H₂O), nickel(II) chloride hexahydrate (NiCl₂.6H₂O), amino tris (methylene phosphonic acid) (ATMP), polyvinylpyrrolidone (PVP₄₀₀₀₀), sodium borohydride (NaBH₄), potassium hydroxide (KOH), methanol, ethanol, toluene, nickel(II) acetylacetonate (Ni(acac)₂), octadecene (ODE), oleylamine (OLAM), trioctylphosphine (TOP), methoxy-polyethylene glycol 5,000 acetic acid (PEG-COOH), iron pentacarbonyl (Fe(CO)₅), nitric acid (70% HNO₃), perfluorinated NafionTM solution, and sulfuric acid (95-97% H₂SO₄) were

purchased from commercial vendors. Ultrapure water (18.2 M Ω , Millipore, Bedford, MA, USA) was obtained from a Milli-Q Integral system. Hydrophilic conductive carbon paper was obtained from Fuel Cell Earth, gold wire was obtained from Sigma Aldrich, and Kapton[®] tape and film was obtained from American Durafilm.

3.2 NP-aq Nanoparticle Synthesis

Fe – Ni nanoparticles were synthesized at room temperature (rt) and under atmospheric pressure conditions. All the solutions were prepared by using ultrapure deionized water as the solvent. As a first step, solutions of 29.79 g.L⁻¹ ATMP and 4.982 g.L⁻¹ of FeSO₄.7H₂O were mixed at a molar ratio of 0.05: 1, while the ATMP compound stabilized the iron cations. Next, the PVP₄₀₀₀₀ (molar ratio of Ni: PVP₄₀₀₀₀ = 1: 0.005) and NiCl₂.6H₂O solutions were prepared for a final theoretical composition of Fe₂₀Ni₈₀. The experimental composition was confirmed by inductively coupled plasma mass spectrometry to be Fe₁₇Ni₈₃. Both solutions were then transferred to a 250 mL threeneck borosilicate flask and mixed under argon gas for 15 minutes at 100 rpm on an orbital shaker. Argon bubbling of the iron-nickel solution is performed to prevent the unwanted oxidation of the Fe and Ni precursors and to control oxidation during nanoparticle formation. At approximately 13 minutes of argon bubbling, NaBH₄ (molar ratio of metal: $BH_4^- = (1: 2.2)$) aqueous solution was prepared to minimize the reaction time of NaBH₄ with water before adding to the iron-nickel precursor solution. The aqueous solution of NaBH₄ was then added into the metal precursor solution in the three-neck flask dropwise via a syringe at a rate of approximately 30 µl.s⁻¹ under continuous mixing. Borohydride ions (BH₄-) reduce the stabilized Fe²⁺ and Ni²⁺ ions into Fe⁰ and Ni⁰, respectively, forming nanoparticles during the reduction reaction. The solution in the threeneck flask was then mixed under vacuum for 15 minutes on an orbital shaker at 100 rpm. After 15 minutes of mixing, the solution in the three-neck flask was transferred to a 50 mL test tube and

centrifuged for approximately 3 minutes. Supernatant from the centrifuged test tube was then decanted. The nanoparticles remaining in the test tube were mixed with 20 mL of 100% methanol in a vortex shaker for about 30 seconds. The test tube containing the solution was again centrifuged for about 3 minutes, and the supernatant was decanted. The nanoparticles were then mixed with 20 mL of methanol and resuspended.

3.3 NP-oil Nanoparticle Synthesis

The Ni – Fe core–shell nanoparticles were synthesized using our previously-established method by a two-step procedure involving the synthesis of a Ni core followed by coating of the Ni core with an Fe shell.²⁵ Briefly, Ni(acac)₂ (51.5 mg, 0.2 mmol), 4 mL of ODE, and 1 mL of OLAM were added to a 3-neck, round bottom flask equipped with a temperature probe, attached to a watercooled condenser under Ar gas flow. This reaction mixture was degassed for 10 min prior to the addition of 1 mL of TOP. Under the protection of Ar, the reaction mixture was heated directly to 220°C and held for an additional 30 min to allow the formation of Ni cores. After the reaction, excess reactants were removed by mixing with toluene/ethanol (1:10 volume ratio) and centrifuged at 8,000 rcf for 5 min. The nanoparticle pellet was dispersed in 3 mL of toluene. For the Fe coating procedure, 1.5 mL of the above Ni nanoparticles (~5 mg) dispersed in toluene was dried under a stream of N₂ in a 3-neck, round-bottom flask, and subsequently dispersed in 200 µL of OLAM and 5 mL of ODE via sonication. The reaction mixture was degassed using Ar then ramped and stabilized at 110°C. At this point, Fe(CO)₅ (20 µL, 0.15 mM?) was injected into the reaction mixture using a 100 µL gas tight syringe. The temperature was then ramped to 200°C at a rate of 2.5 °C.min⁻¹ and held at 200°C for an additional 60 min. The excess reactants were removed by mixing with toluene/ethanol (1:15 volume ratio of the pure solvents) and centrifuged at 8000 rcf for 5 min and then washing by toluene/ethanol (2:1 volume ratio) and collected by centrifuging at

2000 rcf for 5 min. The nanoparticles were dispersed in 2 mL of toluene and transferred to an aqueous solution by a surface ligand exchange process using 10 mL of 1 mg.mL $^{-1}$ PEG-COOH in CHCl₃ for 8 h. The product was purified in 30 mL of 100% hexane and centrifuging at 9,000 rcf for 10 min. The pellet was further purified by ethanol and centrifuged at 14,000 rcf for 60 min, then washed by 18 M Ω H₂O twice, and finally collected by centrifuging at 14,000 rcf for 30 min and dispersed in ethanol for further use.

3.4 Electrochemical Measurements

Step-chronoamperometry (SCA) was performed in the operando electrochemical cell at rt using a potentiostat/galvanostat (PINE WaveNow 50) equipped with AfterMath software in a conventional three electrode system, where conductive carbon paper with a gold wire for electrical connection was used as the working electrode, while a graphite rod (Pine Research) and Ag/AgCl (3 M NaCl, BASi) were used as the counter and reference electrodes, respectively. The backside of the carbon paper electrode was pressed against the Kapton® film to eliminate the interference of electrolyte during the measurement. The potential was ramped in ascending order from 0.0 V to 0.9 V vs. Ag/AgCl and then back down in descending order from the peak potential of 0.9 V to 0.0 V vs. Ag/AgCl at a potential step of 0.1 V. Catalyst inks were prepared for both the samples by combining the nanoparticles with a cationic ionomer (NafionTM) at a mass ratio of 5:1 catalyst to ionomer in methanol. The catalyst mass was determined by ICP-MS characterization of the Ni and Fe content, and the catalyst ink concentrations were normalized to 2 mg.mL⁻¹. The ink was then sonicated for 45 minutes in a cold-water bath to ensure a homogeneous mixture of the nanoparticle and the ionomer. The ink was then drop casted on the surface of the carbon paper (surface area of 1cm^2) 50 µL at a time, allowing each aliquot dry in air for 15 minutes at rt. This process was repeated 10 times until the final mass loading on the electrode surface was ~1 mg.cm⁻²

The electrochemical measurements were performed in 1 M KOH electrolyte (pH = 14) which were purified to remove trace iron impurities based on a procedure developed by Trotochaud et al.⁷ Prior to KOH purification, all the glassware and polypropylene centrifuge tubes were cleaned with 10 % sulfuric acid (H₂SO₄) solution and rinsed with de-ionized H₂O. Then, 2 g of nickel nitrate hexahydrate (Ni(NO₃)₂·6H₂O) was dissolved with 4 mL of 18.2 MΩ DI H₂O in a tube, and 20 ml of 1 M KOH was added together and mixed to obtain nickel hydroxide (Ni(OH)₂) as a precipitate. The mixture was then shaken using a vortex shaker for approximately 1 minute and centrifuged for 15 minutes at 7,800 rpm. The supernatant was emptied from the tube, and three more cycles of washing Ni(OH)₂ precipitate with 20 mL H₂O and 2 mL of 1 M KOH were employed with each wash cycle followed by re-dispersion, centrifugation, and supernatant decantation successively. After the 3rd cycle was completed, 50 mL of 1 M KOH electrolyte to be purified was added into the tube, and the pellet was dispersed via sonication and vortexed for 10 minutes ensuring complete dispersion. The mixture was then allowed to rest for 3 hours for iron impurity removal, after which the solution was centrifuged, and the purified 1 M KOH supernatant was decanted into an H₂SO₄cleaned tube.

3.5 X-ray Absorption Spectroscopy Data Collection and Analysis

X-ray absorption spectroscopy (XAS) was performed on the catalysts at beamline 9-3 of the Stanford Synchrotron Radiation Lightsource (SSRL) at SLAC National Accelerator Laboratory. The dry samples and standards were prepared by drop-casting 50 µL of a 1 mg.mL⁻¹ suspension of the sample/standard in methanol on the sticky side of Kapton[®] tape. This was air-dried before sealing the sample with another piece of Kapton[®] tape over the top. The in-situ electrodes were

prepared by drop-casting 1 mL of the nanoparticle ink on a 1 x 1 cm² area on hydrophilic carbon paper. The ink concentration was standardized to 1 mg.mL⁻¹ (mass of Ni and Fe) and prepared with a 1:5 Nafion to catalyst mass ratio in 100% methanol. An operando electrocatalysis cell specifically designed for XAS experiments was used to characterize the Fe – Ni nanoparticles. The CAD illustrations and pictures of the in-situ cell are shown in Figure S1. The in-situ cell was designed using FreeCAD software and fabricated using a 3D printer using acrylonitrile butadiene styrene (ABS). Polyimide Kapton® film (75 µm thickness) was used as the window material. The working electrodes containing the catalysts were loaded into the in-situ cell at a 45° angle to the incident x-ray beam. Fluorescence XAS data was collected while running electrochemical experiments simultaneously, thus were true operando measurements. The measurements were conducted at the K-edge of Fe (7,112 eV) and K-edge of Ni (8,333 eV), respectively. Continuousscanning XAS with a passivated implanted planar silicon (PIPS) diode was used to collect fluorescence XAS data at a 90° angle relative to the incident x-ray beam. Fe and Ni foil references were scanned simultaneously for energy calibration. Data analysis was done using the Demeter software package.⁴⁰

3.6 XAS Data Analysis and Modeling

Extended x-ray absorption fine structure (EXAFS) modeling was accomplished using Artemis from the Demeter software package,⁴⁰ where E_0 values of 7,112 eV for Fe K-edge and 8,333 eV for Ni K-edge were used. Continuous Cauchy wavelet transforms (CCWT) were calculated using the CCWT function in the Larch software package.⁴¹ All CCWT calculations were performed with a k-range of 0-12 Å⁻¹ and an R-range of 0-6 Å.

EXAFS models were optimized in R-space using k^1 , k^2 , and k^3 weightings, with all models obeying the Nyquist criterion. γ -FeOOH was used as the base structure to build the model upon. ¹¹

Phase functions were also generated from Fe and Ni metal structures to accommodate for the metallic scattering paths. For the Fe K-edge analysis, Fe was the absorber atom whereas for the Ni K-edge, all the Fe atoms of γ -FeOOH were replaced by Ni atoms in the FEFF input file to generate an appropriate structure. An amplitude reduction factor, S_0^2 , of 0.85 was used for both Fe and Ni K-edges as a reasonable estimate for our system. Prior studies on FeNiO(H)_x materials have also used an amplitude reduction factor of 0.85. 31 S_0^2 values in relevant literature range from 0.70 – 0.85.11, 27, 31 Thus, while the absolute values of the coordination number values may differ, as we report below, the trends observed with applied potential align with prior studies. The following Fourier transform parameters were utilized for the fitting process: $k_{min} = 3.0 \text{ Å}^{-1}$, $k_{max} = 12 \text{ Å}^{-1}$, dk= 1, r_{min} = 1 Å, r_{max} = 3.2 Å, and dr =0. Phase correction was not done, and $\varepsilon(k)$ was kept at 0. Simultaneous fits were carried out for dry, 0 V anodic, 0.9 V, and 0 V cathodic samples for NPaq and NP-oil at both the Fe and Ni K-edges. ΔE_0 was set to be the same for all, whereas coordination number (CN), ΔR , and σ^2 factors were left as guess parameters. Simultaneous fitting was applied to obtain the results shown in Tables S1 – S4, Figure S10, and the figures presented later in this paper. For the results shown in the SI, (Tables S5 – S11 and Figure S13 – S20), each spectrum was individually fitted. ΔE_0 was also left as a guess parameter along with CN, ΔR , and σ^2 factors.

Pre-edge peaks of the normalized XANES spectra were analyzed using MATLAB codes based on work done by Boubnov et al.³² Edge positions of the reference foils for Fe and Ni were set at 7,112 eV and 8,333 eV, respectively. Background subtraction was carefully done around the pre-edge region to isolate the pre-edge peak. The background-subtracted pre-edge regions were then fitted using multiple sets of pseudo-Voight peaks ranging from 1 to 5. The peak integration values reported in this paper were chosen based on the quality of fit, preliminary knowledge of the

expected number of electronic transitions as well as the peak width and a Gaussian fraction consistent with the instrumental resolution.

4. Results and Discussion

4.1 Operando OER Electrochemical Conditions

For this operando study, XAS spectra were obtained for an anodic SCA voltage step series and for a cathodic SCA voltage step series, where during the entire anodic voltage ramp and cathodic voltage ramp, the applied voltage was never allowed to return to open circuit voltage (OCV). The anodic and cathodic ramps were performed sequentially on the same sample for both NP-aq and NP-oil nanoparticle catalysts. For each SCA experiment, the applied voltage was held for as long as was needed for each scan sequence (90 seconds/scan × 9 scans per voltage step), and the voltage was increased stepwise by 0.1 V from 0.0 V to 0.9 V vs. Ag/AgCl, then decreased stepwise back down to 0.0 V vs. Ag/AgCl. Operando XAS spectra were collected at the Fe K-edge and the Ni K-edge for both NP-aq and NP-oil nanoparticle materials as a function of applied voltage in a custom 3-D printed spectro-electrochemistry cell, see Figure S1. Both nanoparticle samples, NPaq and NP-oil, were previously characterized in detail by dry, ex-situ methods and these results are reported elsewhere. ^{20,25} In addition, extensive electrochemical characterization was previously performed to assess the electrocatalytic activity of these two nanoparticle materials for the OER, with results also reported previously. ^{20, 25, 38-39} In these prior works, we have extensively studied the surface chemistry, particle morphology, particle composition, and electrocatalyst performance, and the reader will find results that include x-ray photoelectron spectroscopy (XPS), x-ray diffraction (XRD), transmission electron microscopy (TEM), and energy dispersive x-ray spectroscopy (EDS). We report a summary of TEM results in Figure S2 refer the reader to these previous papers, and we report a set of comparative cyclic voltammograms (Figure 1; Figure S3)

to assess electrocatalytic OER performance. The results shown in Figure 1 are similar to those reported and are comparable to best-performing FeNiO(H)_x electrocatalysts reported in recent literature. ^{12, 42} In Figure 1, a comparison of the two nanoparticle electrocatalysts shows that, after the 1st cyclic voltammetry (CV) cycle, the NP-aq sample results in larger measured current densities in the OER Faradaic region, as compared to the NP-oil sample. However, the onset of OER activity is similar for both nanoparticle catalysts. Further, both electrocatalysts result in improved OER activity and eventual stabilized performance with cycling. Based on the previous structural analysis, Figure S4 depicts the possible paths of the EXAFS modeling (metallic versus oxide/hydroxide).

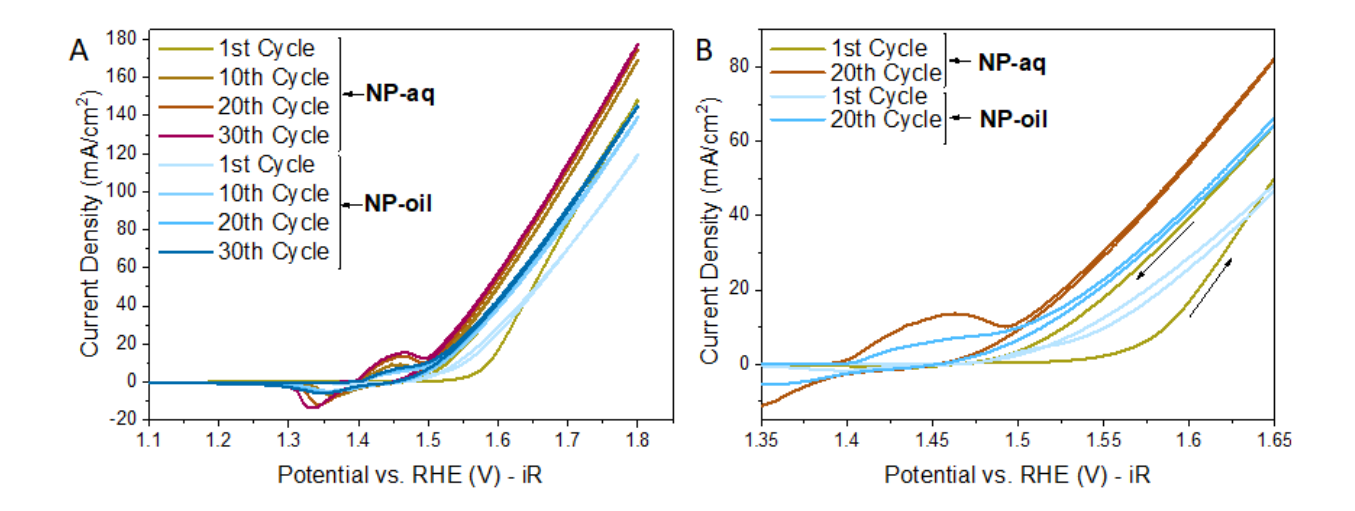


Figure 1. Electrocatalytic performance of NP-aq and NP-oil shown for the (a) first, tenth, twentieth, and thirtieth cycles at full voltage scan range and (b) the first and twentieth cycles for the voltage range around the nickel redox feature and onset of OER current. CVs were performed in 1 M purified KOH.

An analysis of the CV dataset shows that both nanoparticle electrocatalysts resulted in nearly identical overpotentials at 10 mV/cm², where the NP-aq catalyst resulted in 262 mV overpotential while the NP-oil catalyst resulted in 271 mV overpotential. However, based on the difference in observed slopes of the current response, it is possible that the overpotentials of the two catalysts would vary to a much larger extent at higher current densities that are more relevant to electrolysis. In addition, a Tafel analysis (Figure S5A) showed that the NP-aq catalyst resulted in lower Tafel slopes at low overpotential region (i.e., 119 mV.dec⁻¹ for NP-aq and 146 mV.dec⁻¹ for NP-oil); the trend was similar at higher overpotentials. Despite challenges in using CV data for Tafel analysis, 43 the comparison here suggests that the NP-aq catalyst has improved activity, as compared to the NP-oil catalyst. Chronopotentiometric data were analyzed to quantify the catalyst voltage degradation rate (Figure S5B), and results show that NP-aq has a lower degradation rate of 1.36 mV.hr⁻¹, compared to NP-oil at 7.26 mV.hr⁻¹. We note that the CV data for both nanoparticle electrocatalysts were obtained on carbon paper electrodes in a standard laboratory three-electrode cell prior to testing in the operando spectroscopy cell. The differences in Tafel slope determined in this study, as compared to our prior studies, 20, 25 are due to the difference in current collector (i.e., carbon paper vs. glassy carbon or gold electrode).

4. 2 Fe K-edge and Ni K-edge operando XANES

The XANES and pre-edge regions of NP-aq and NP-oil nanoparticles during both the anodic and cathodic ramps at the Fe K-edge are shown in Figure 2. Data for the dry NP-aq and NP-oil samples are shown in Figure S6. For the NP-aq nanoparticle catalyst (Figure 2A, B), the Fe K-edge XANES spectra from 0.0 V to 0.7 V vs. Ag/AgCl (1.02 – 1.72 V vs. RHE) are static while a slight peak shift to higher absorption energy is observed at 0.8 V vs. Ag/AgCl (1.82 V vs. RHE) (Figure 2A).

In addition, the pre-edge region of the Fe K-edge at 0.8 V also changed (Figure 2A, inset). The peak shift to higher absorption energy is reversed (Figure 2B), and the pre-edge distortion also reverses after 0.6 V vs. Ag/AgCl is reached, during the cathodic ramp. There is a clear distinction between the position of the 0.9 V, 0.8 V, and 0.7 V vs. Ag/AgCl spectra and the rest of the spectra during the cathodic ramp. The same SCA experiments were performed on the NP-oil nanoparticle sample; however, the potential hold series caused a more subtle shift in the edge and pre-edge, as seen in Figure 2C, D. These results suggest that structural changes to both the Fe and Ni species of these electrocatalysts do not occur until the applied voltage is well into the Faradaic regime of the OER (i.e., above 1.7 V vs. RHE).

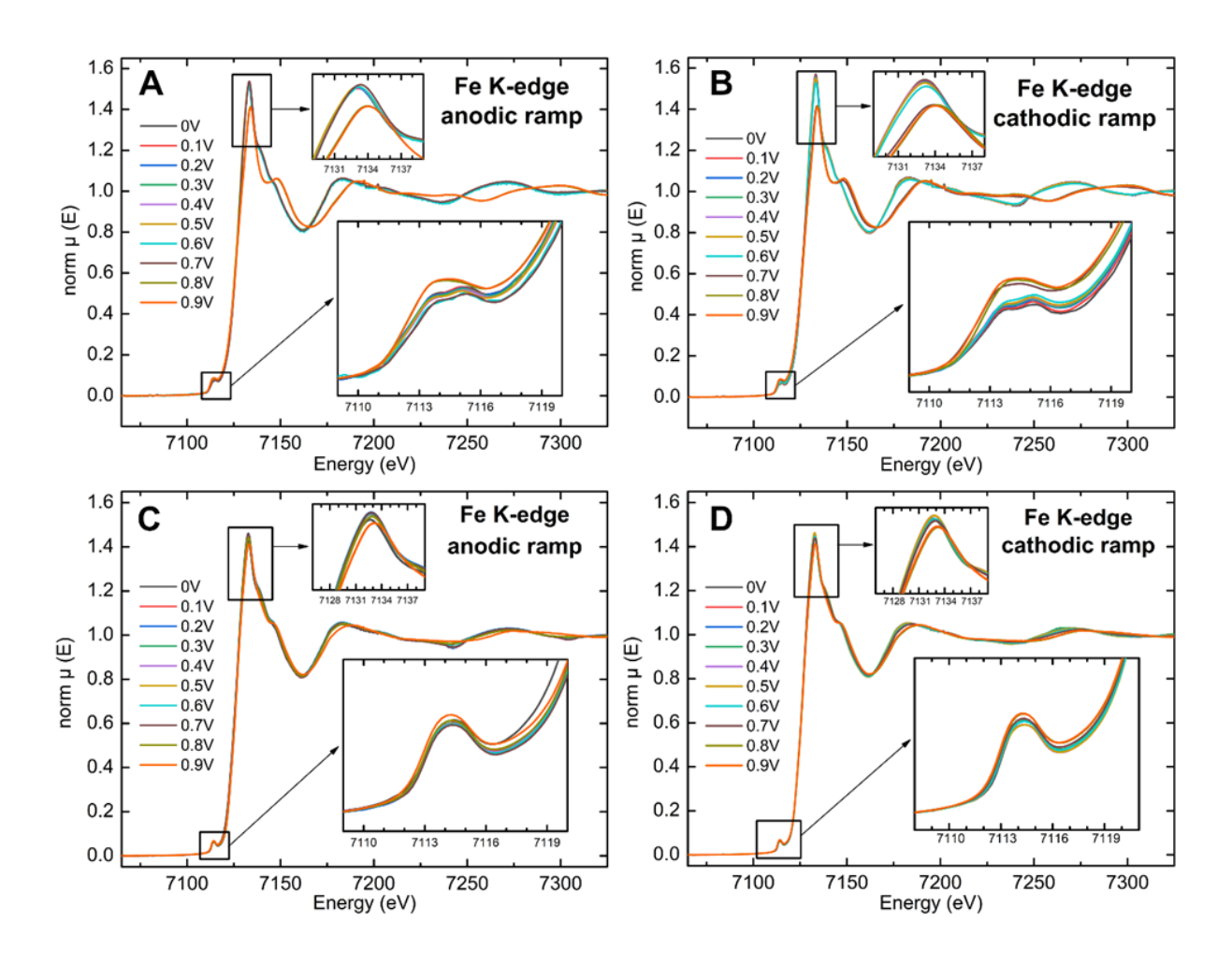


Figure 2. XANES spectra obtained at the Fe K-edge in purified 1.0 M KOH (pH 14.0) for NP-aq catalyst: (A) anodic ramp from 0 V to 0.9 V vs. Ag/AgCl (3 M NaCl), (B) cathodic ramp from 0.9 V to 0.0 V vs. Ag/AgCl; and for NP-oil catalyst: (C) anodic ramp, (D) cathodic ramp under the same electrochemical conditions as the NP-aq sample. The insets of each graph show a zoomed-in view of the pre-edge and white line regions.

The distinct doublet structure seen in the pre-edge of the Fe K-edge³² for NP-aq suggests a coordination environment similar to that of γ -FeOOH or Fe₂O₃, where iron is in a +3 octahedral (O_h) state on iron-nickel hydroxide films.¹¹ At the highest voltage, the doublet feature of the NPaq disappeared to give rise to a single broad peak. In addition, the intensity of the pre-edge peak feature increases slightly. The increase in pre-edge peak intensity suggests a change in coordination state, as coordination environments with centrosymmetric geometry (e.g., Oh) have lower pre-edge intensity as a result of the weaker quadrupole transition 36 1s \rightarrow 3d contribution to the pre-edge feature;³² non-centrosymmetric coordination environments of the metal tend to result in higher intensity pre-edge features. In the case of Fe, the $s \rightarrow p$ transition energy increases as the effective nuclear charge on the metal increases.³² In addition, mixing between Fe 3d and 4p orbitals is thought to lead to enhanced dipole transitions (i.e., $s \to p$), ³⁶ which have higher intensity preedge features³² and which can contribute to the pre-edge peaks (e.g., in Chen et al., 44 dipole transitions contribute to the second pre-edge peak). In other words, a reduction in the coordination number of the Fe species $^{33-37,45}$ as well as increased metal p character in the Fe d-band, 33,36,46 noncentrosymmetric coordination, ³⁶ and decreased Fe – O covalency ³⁵⁻³⁶ resulted in an increase in the pre-edge peak intensity, 32-33, 35-36 and is thus what we conclude occurs for the Fe species in the NPaq at higher applied voltages. The increase in the pre-edge peak intensity also suggests the lack of Fe⁴⁺ formed under OER voltages, as the Fe⁴⁺ – O²⁻ bond is expected to have greater covalency (and thus cause a decrease in Fe pre-edge peak intensity) than the Fe³⁺ – O⁻ pair.³⁵ This qualitative assessment is further confirmed below through pre-edge analysis and EXAFS fitting. Interestingly, the spectra for the NP-oil at the pre-edge of the Fe K-edge did not show a doublet feature, nor did the spectra change significantly as a function of voltage, suggesting a dominated, fairly-stable Fe³⁺ non-centrosymmetric coordination environment,³⁶ likely existing in a distorted octahedral state.³²

The Ni K-edge XANES and pre-edge regions of NP-aq and NP-oil during both the anodic and cathodic ramps are shown in Figure 3. For both samples, the Ni absorption edge and pre-edge features shift towards higher absorption energy as the applied voltage increases into the OER Faradaic regime. For the NP-aq, the spectral shape remains static during the anodic ramp from 0.0 to 0.7 V vs. Ag/AgCl (1.02 – 1.72 V vs. RHE), begins to shift towards higher energy starting at 0.8 V (1.82 V vs. RHE), moves slightly further at 0.9 V (1.92 V vs. RHE), then remains in that state during the cathodic ramp before returning to its original shape at 0.6 V vs. Ag/AgCl, as seen in Figure 3A, B. The Ni K-edge for the NP-oil shows similar behavior, as seen in Figure 3C, D, but the magnitude of the shift in the absorption edge to higher absorption energy is less than that of the NP-aq. Similar to the results for the Fe K-edge, significant structural change does not occur until well into the Faradaic regime of the OER. These results generally align with prior literature reports of operando Ni K-edge spectroscopy studies, 11, 27, 29, 47-48 except for that of Abbott et al.; 12 however, they evaluated a limited applied potential range of 1.2 V - 1.65 V vs. RHE, and perhaps the applied potential was not high enough to cause a shift in the Ni K-edge absorption energy. We cannot rule out the role of the catalyst morphology, where the study of Abbott et al. 12 is one of the few to probe FeNiO(H)_x nanoparticles by operando XAS, in comparison to those that have studied FeNiO(H)_x films. In comparison, the results shown in the present study were performed on

nanoparticles but at a larger voltage range of 1.02 - 1.92 V vs. RHE (NB: conversion from Ag/AgCl reference electrode to RHE = $0.059*pH + E^0_{SHE}$ (0.197 V) + $E_{Ag/AgCl}$). Given the changes that are observed in both the Ni K-edge and the Fe K-edge, the role of catalyst morphology remains to be further explored.

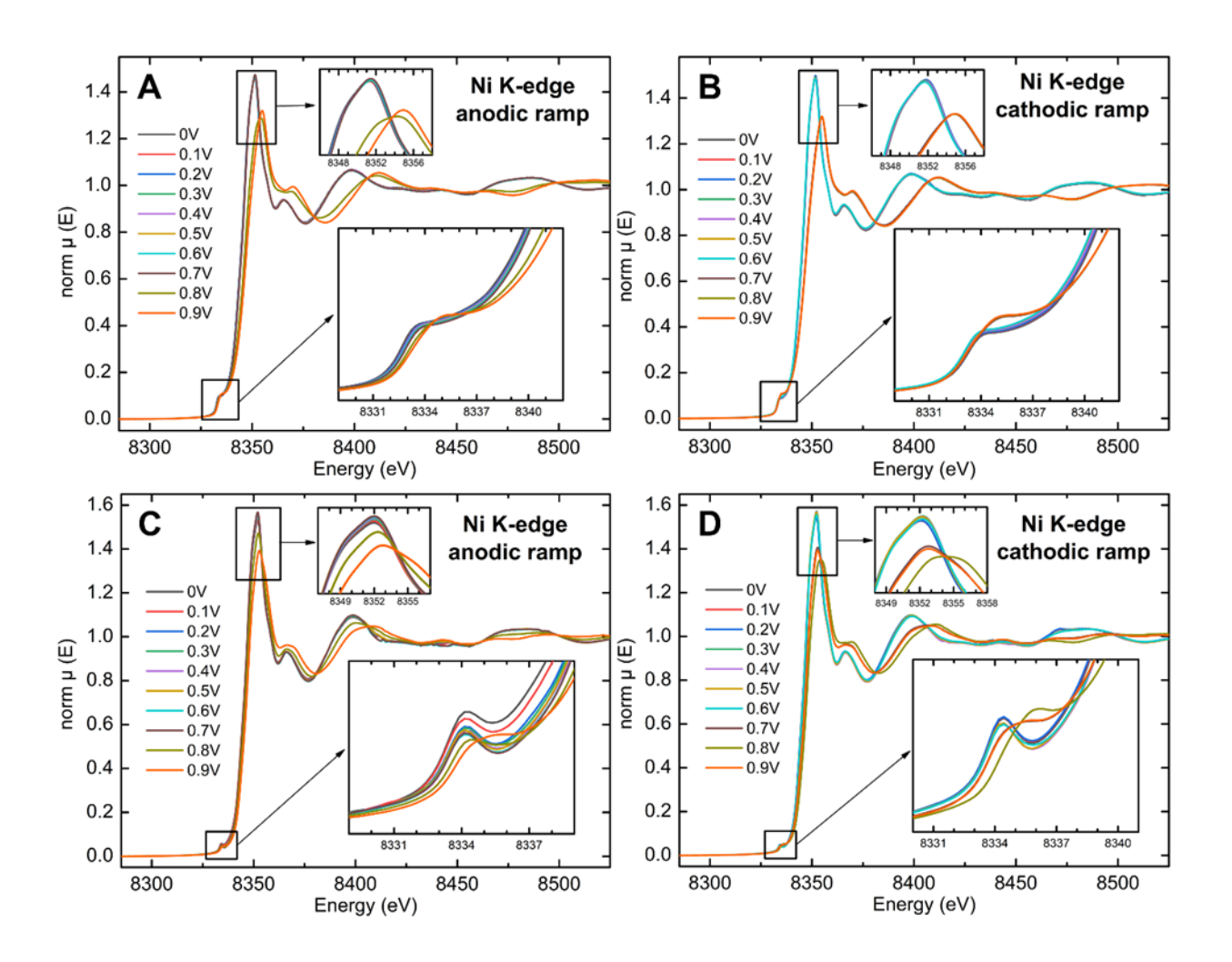


Figure 3. XANES spectra obtained at the Ni K-edge in purified 1.0 M KOH (pH 14.0) for NP-aq catalyst: (A) anodic ramp from 0 V to 0.9 V vs. Ag/AgCl (3 M NaCl), (B) cathodic ramp from 0.9 V to 0.0 V vs. Ag/AgCl; and for NP-oil catalyst: (C) anodic ramp, (D) cathodic ramp under the

same electrochemical conditions as the NP-aq sample. The insets of each graph show a zoomedin view of the pre-edge and white line regions.

Multiple in-situ XAS studies have shown Fe and Ni primarily exist in +3 and +2 oxidation states, respectively, in a bimetallic FeNiO(H)_x system.⁴⁹⁻⁵¹ Similar results have been observed here for both as-synthesized NP-aq and NP-oil despite a difference in synthesis approaches.^{20, 25} The weak pre-edge features seen for both NP-aq and NP-oil at the Ni-K edge agree with a 1s \rightarrow 3d electronic transition that is most commonly associated with octahedral geometry.⁵²⁻⁵³ However, the case can be made for Ni being in a distorted octahedral geometry.⁵⁰ McBreen et al. suggested that in the case of pure octahedral coordination, no pre-edge peak should be observed, and as such, the weak pre-edge feature is the result of distortion in the coordination geometry.⁵⁴ It appears that the Ni species in the NP-oil may be in a more distorted octahedral geometry than the Ni species in the NP-aq, due to the more intense pre-edge peak height. In the Ni K-edge, both NP-oil and NP-aq showed an increase in the oxidation state of Ni at higher potentials. The Ni species, which are present in the +2 oxidation state in the as-synthesized nanoparticles, transform to a +3/+4 state in the OER Faradaic region, mirroring the transformation of α-Ni(OH)₂ to γ-NiOOH in previous work on thin films.^{12, 47, 50, 53}

4.3 Pre-edge Analysis of Fe K-edge and Ni K-edge XANES Spectra

Analysis of the pre-edge centroid, following the approach of Boubnov et al.,³² was performed for both the Fe K-edge and the Ni K-edge of experimental spectra obtained for both nanoparticle samples and compared to reference materials. Data for the four Fe reference materials (i.e., Fe²⁺ T_d : Staurolite; Fe²⁺ O_h : Olivine; Fe³⁺ T_d : Sanidine; Fe³⁺ O_h : Aegirine; shown as encircled black squares in Figure 4A) were obtained based on the work and MATLAB codes created by Boubnov et al.³² Centroid results for the Fe K-pre-edge (Figure 4A) suggest that the Fe species in the NP-

oil, as the catalyst is taken from the dry environment to the electrochemical environment at 0.0 V vs. Ag/AgCl, and then stepped up to 0.9 V vs. Ag/AgCl and back down to 0.0 V vs. Ag/AgCl, largely remains in a +3 octahedral state. Despite not observing the characteristic two-peak lowintensity feature for Fe^{3+} O_h , the Fe species in the NP-oil appears to be quite similar in coordination environment to the Fe^{3+} O_h reference material, aggirine. In contrast, the peak intensity of the preedge centroid varies with the applied environment for the NP-aq, where the Fe species appears to shift in coordination environment between distorted O_h and nearly T_d . The dry, as-synthesized NPaq contained a FeNi alloy metallic core surrounded by a FeNiO_x shell,²⁰ where at ambient temperature, the alloy would be expected to be primarily in a bcc phase. 55-56 This metal component of the as-synthesized NP-aq likely influences the centroid energy and integrated peak intensity calculations of the pre-edge features. In comparison, once the NP-aq are under applied voltage, the Fe species shift toward octahedral coordination, suggesting a larger portion of the Fe atoms in the nanoparticles are likely oxidized Fe³⁺. Interestingly, at 0.9 V vs. Ag/AgCl, the Fe species appear to shift toward Fe^{3+} T_d , suggesting the possible formation of tetrahedral Fe species during OER. It has recently been suggested that iron species of a FeNiO(H)_x electrocatalyst may transition between octahedral and tetrahedral coordination when an OER Faradaic voltage is applied,²⁹ and that this transition in coordination environment is critical to the active site structure of a highly active OER electrocatalyst. Few other operando XAS studies on FeNiO(H)_x electrocatalysts report or discuss Fe K-pre-edge data, due possibly to a lack of spectral resolution of the subtle features of the pre-edge and/or due to a lack of knowledge or understanding of how to quantitatively interpret the pre-edge features. For example, in the detailed and thorough work of Friebel et al., 11 the authors graphically reported the details of the Fe and Ni K-pre-edges, but the spectral resolution obtained during operando XAS experiments was not sufficient to conduct a further detailed

analysis. Friebel et al.¹¹ do report a decrease in the coordination number for the Fe species under applied OER voltages, which the authors conclude may indicate that a similar $O_h \to T_d$ shift in coordination geometry occurred in their FeNiO(H)_x films. Further studies that can resolve preedge features during operando XAS experiments are thus warranted to understand whether this transition in coordination geometry is observed in other FeNiO(H)_x, and if so, whether this transition is indeed correlated to more highly active OER electrocatalysts. In the present study, we can conclude that the $O_h \to T_d$ shift is observed for the more active and stable NP-aq electrocatalyst, suggesting a possible correlation between NP synthesis route, NP structure, and OER performance metrics.

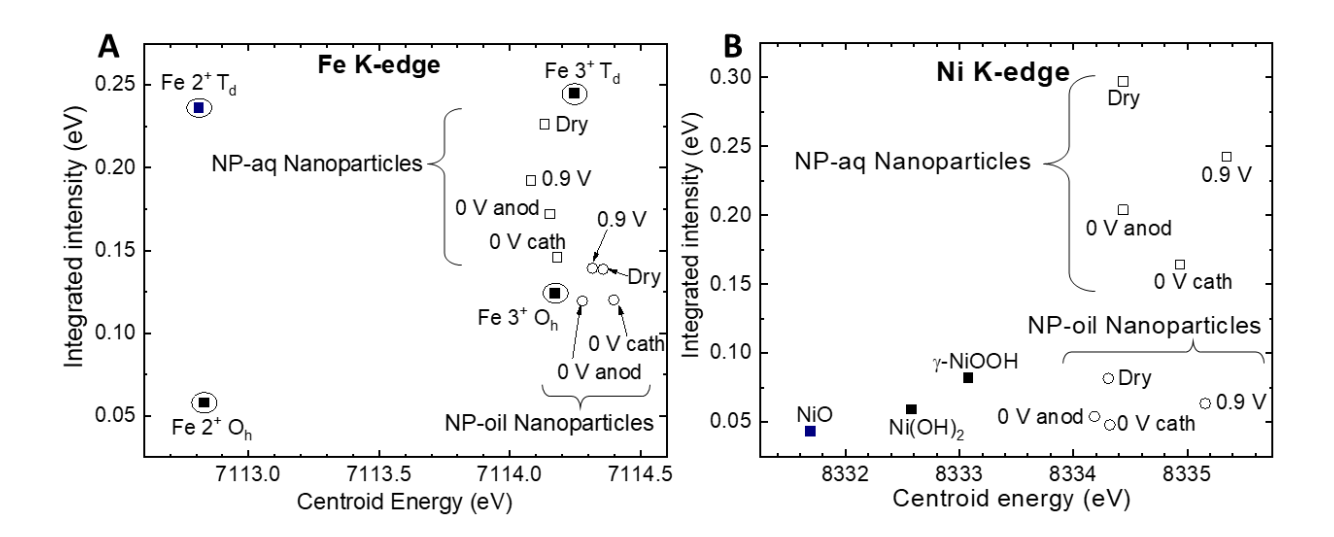


Figure 4. (A) Fe K-edge comparison of the calculated centroid energy positions of the pre-edge. (B) Ni K-edge comparison of the calculated centroid energy positions of the pre-edge. Abbreviations are as follows: Octahedral (O_h); tetrahedral (T_d); Anodic SCA series (anod); Cathodic SCA series (cath); NiO_x-FeNiO_x nanoparticles (NP-aq, open squares); FeNiO_x alloy nanoparticles (NP-oil, open circles).

The results for the Ni pre-edge analysis (Figure 4B) show that NP-oil result in similar integrated peak intensities to the Ni reference materials as well as for the different dry and electrochemical environments, but the calculated centroid energy is larger than that of the references. In contrast, an analysis of the NP-aq shows that, similar to the Fe pre-edge, the change in environmental conditions causes larger changes in integrated peak intensity, as compared to the NP-oil. These results could suggest Ni coordination shifts with applied potential and unique chemical environments because of the nanoscale structure of the nanoparticles, as compared to bulk phase reference materials. Both NP-aq and NP-oil result in an increase in the Ni pre-edge centroid peak position at 0.9 V vs. Ag/AgCl, suggesting that for both catalysts, the Ni oxidation state increases under OER voltages.

4.4 Linear Combination Fitting of XANES Data

To quantify the results obtained with the XANES data during SCA, linear combination fitting (LCF) was performed on the samples. Traditional LCF analysis was performed with several standard reference materials for both the Fe K-edge and the Ni K-edge (see Figure S7); however, the analysis erroneously suggests an increase in metallic Fe and Ni contributions at higher voltages. This result, while incorrect, points to likely differences in the atomic-scale structure of Fe and Ni in both the NP-aq and the NP-oil, as compared to the bulk reference materials, where it is not possible to conduct a simple LCF analysis because the underlying structures of the nanomaterials are distinct from the bulk materials. As a result, we then conducted a simplified "phase analysis" of the spectra for NP-aq and NP-oil, where we used LCF to track the relative change in "phase" or structure as a function of applied voltage; results for the Fe K-edge are shown in Figure 5.

The spectrum at the initial voltage (0.0 V vs. Ag/AgCl) is considered as the initial phase, and the spectrum of the final voltage (0.9 V vs. Ag/AgCl) is assigned as the final phase. The NP-aq sample during the anodic ramp (Figure 5A) from 0 V to 0.5 V remains unaffected and is similar to that of the initial stage of the electrochemical experiment. A large change occurs between 0.7 V and 0.8 V, where the primary component of the sample resembles that of the final state. During the cathodic ramp (Figure 5B), the majority of the structural change in the NP-aq appears to occur between 0.7 V and 0.6 V, and the remaining small component of the final phase remains as a contribution to the overall structure until the voltage reaches 0.1 V. The results in Figure 5A, B indicate that once the Fe species in the NP-aq are exposed to the high voltages of 0.8 – 0.9 V, the shift in structure back to the original "phase" requires a longer time and/or a lower cathodic ramp voltage, than that required for the structural shift that occurs during the anodic ramp. In the case of the NP-oil, the voltage dependency of structural shifts is drastically different. At a low voltage

of 0.1 V during the anodic ramp (Figure 5C), the sample shifts to almost 40% of the final Fe phase, with a subsequent steady shift toward the final phase, but a higher voltage of 0.9 V is required to completely shift the structure. In contrast, during the cathodic ramp, the NP-oil appear to revert to 100% of the initial phase by 0.5 V, with the shift from final to initial phase starting at 0.8 V. Overall, these results comparing NP-aq and NP-oil and the voltage-dependency of structural shifts suggest that the two nanoparticle catalysts have distinct voltage-structure behavior that is unique and likely connected to the as-synthesized structures of the two nanoparticle materials.

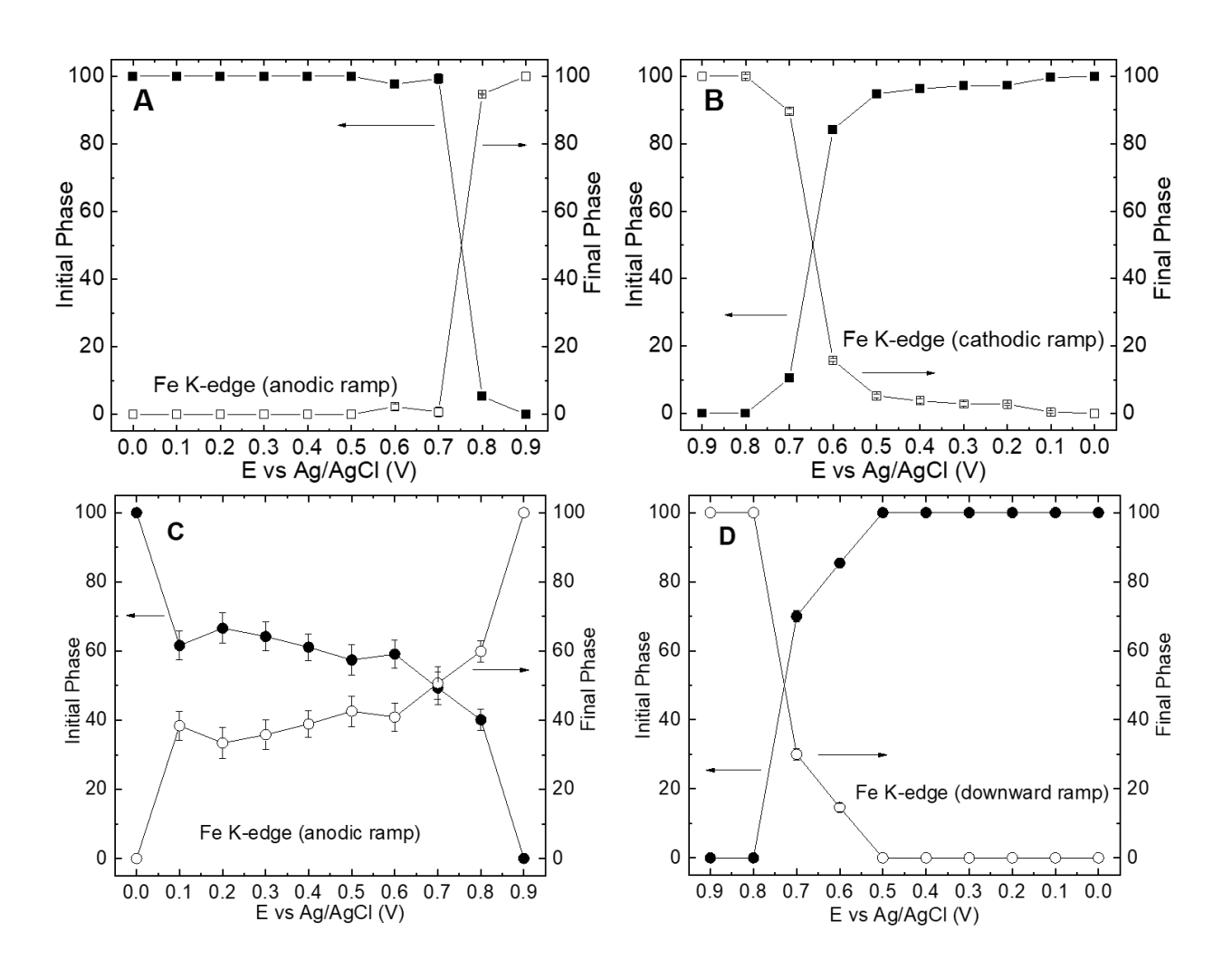


Figure 5. LCF results at the Fe K edge for: (A) NP-aq anodic ramp, (B) NP-aq cathodic ramp, (C) NP-oil anodic ramp, and (D) NP-oil cathodic ramp.

LCF was also conducted on the Ni K-edge for NP-aq and NP-oil. During the anodic ramp (Figure 6A), the NP-aq nanoparticle structure begins to shift with a minor final structural component present at much lower potentials. However, even at 0.8 V, the sample is still about 20% of the initial phase. During the cathodic ramp (Figure 6B), the Ni species in the NP-aq sample completely reverts to the initial phase at 0.6 V, unlike that of the Fe species as seen in Figure 5B. In the case of NP-oil, the trend in Ni K-edge (Figure 6C) is much more abrupt as the sample is 100% in its initial phase until the transition between 0.7 V and 0.9 V, while the cathodic ramp (Figure 6D)

shows the sample reverting to initial state by 0.5 V. For both nanoparticle samples, there are striking differences not only between the two nanoparticle materials, but between the voltage-structure behavior of the Fe versus the Ni species in the same sample.

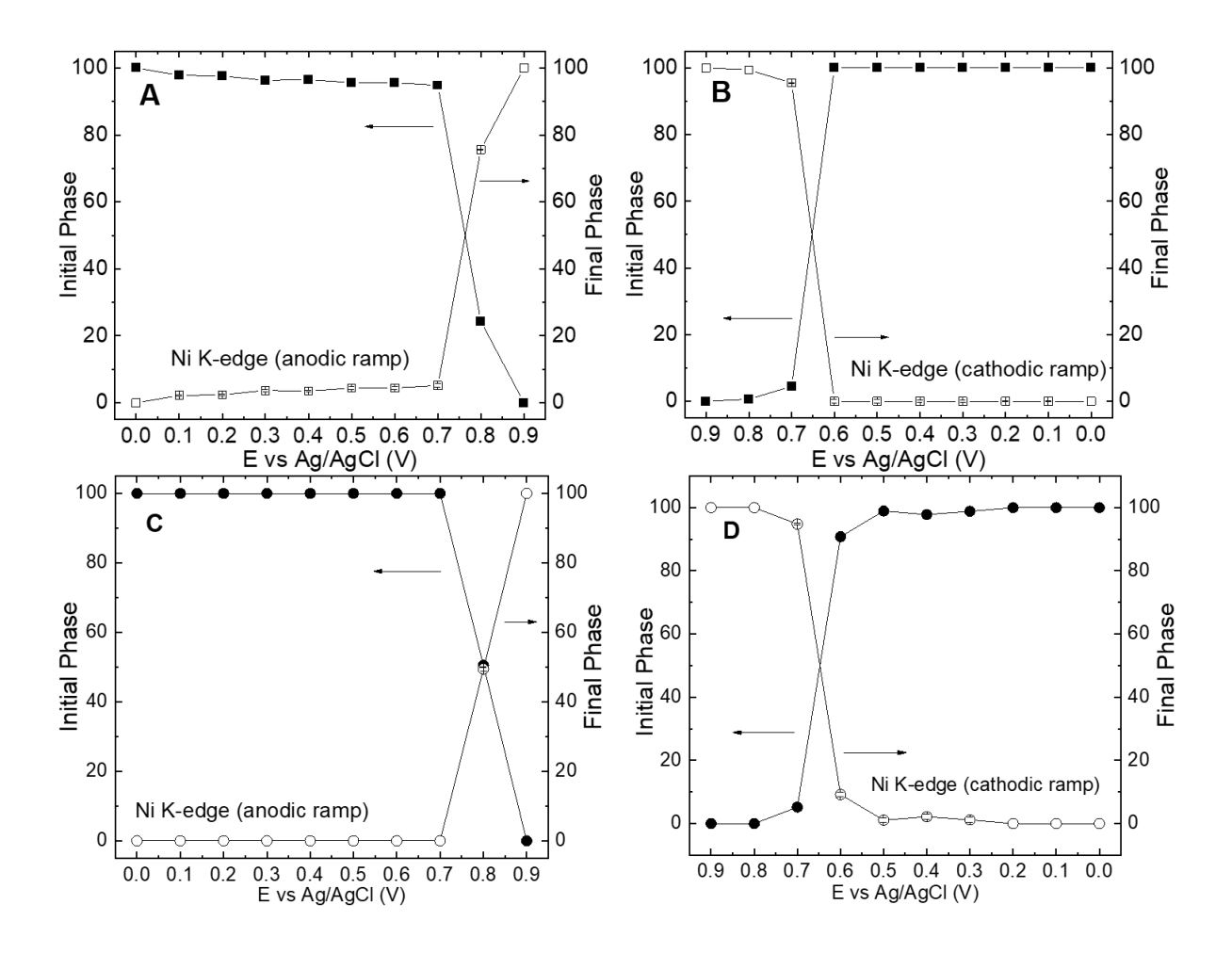


Figure 6. LCF results at Ni K-edge for: (A) NP-aq anodic ramp, (B) NP-aq cathodic ramp, (C) NP-oil anodic ramp, and (D) NP-oil cathodic ramp.

4.5 Analysis of Fe and Ni Oxidation State

Several studies have analyzed the absorption energy position of the Fe K-edge and the Ni K-edge to evaluate the expected oxidation state of both species in FeNiO(H)_x electrocatalyst materials. Cai

et al. report an estimated 22% Fe(IV) at 1.5 V vs. RHE. 16 Gonzalez-Flores et al. 27 also analyzed the shift in Fe K-edge position with applied potential and found a 0.4 eV increase in edge energy above applied potentials of 1.8 V vs. RHE. Although this shift is small and may be due to changes in K-edge shape as a result of changes in the Fe(III) coordination environment, the authors also suggest that the formation of Fe(IV) is possible (~8% of Fe atoms predicted to be Fe(IV)).²⁷ We have analyzed the edge energy at 0.5 of the normalized edge intensity, as well as plotted data from across the literature. Data are plotted in Figure 7A-C for the Fe K-edge based on a set of experimentally measured reference materials (i.e., FeO, Fe₂O₃, and Fe₃O₄) and the linear correlation determined based on these known phase oxidation states for Fe (Figure S8A). The literature comparison in Figure 7A demonstrates that while there is a general correlation between K-edge energy and oxidation state, the quantitative values for the edge position vary among literature reports, and an absolute quantification of the oxidation state based on edge energy is perhaps an over extension of the spectral analysis. However, it is informative to compare within a sample set or within an experimental and reference materials suite to draw qualitative conclusions about oxidation state, as observed in Figure 7B, C. For both NP-aq and NP-oil, the edge position was shifted to slightly higher energy, as compared to the Fe³⁺ reference Fe₂O₃, suggesting possible minor contribution of Fe⁴⁺ species, but edge positions can also shift due to changes in structural environment that are not a result of a nominal change in oxidation state.

A similar analysis was performed for the Ni K-edge for a range of literature values, along with the NP-aq and NP-oil nanoparticle spectral data and associated reference materials (Figure S8B), as shown in Figure 7D-F. The data from reported literature suggest similar to those for Fe, that there is a range of edge energies associated with the +3/+4 oxidation state that is thought to exist under applied voltages in the OER Faradaic regime. This group of data is generally distinct in edge

energy from references known to be in the +2 oxidation state. However, within the group under applied voltage, it is again difficult to quantify precise differences or to know whether these differences are a result of different fractions of the Ni species existing in the +3/+4 oxidation state or whether there are other factors, such as catalyst morphology affecting the results. In the analysis of NP-aq and NP-oil, we do observe a distinct difference in edge energy at higher applied voltages of 0.8 V and 0.9 V, suggesting a higher oxidation state closer to +4 and separated from the data grouping from intermediate applied potentials. The data set obtained at intermediate applied potentials is also distinct from the dry and wet NP-aq and NP-oil that were not under applied potential, suggesting real changes to the Ni species when the catalyst is moved from a dry/wet environment to under applied potential, and subsequently to higher applied potentials. These results further support that this approach can be used within a sample set to compare relative differences, while an absolute quantification of oxidation state is not possible.

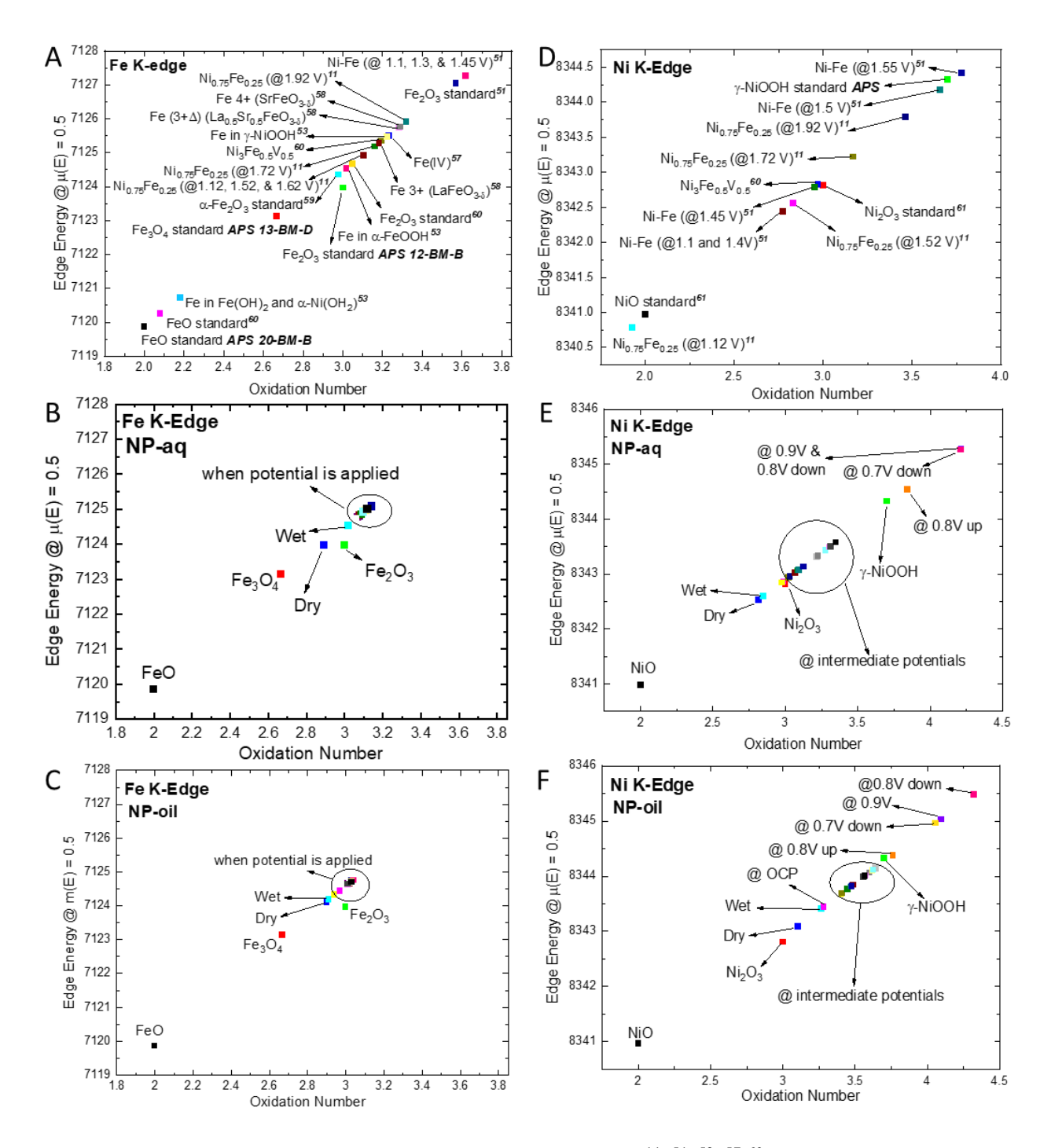


Figure 7. (A) Fe K-edge oxidation numbers from literature, ^{11, 51, 53, 57-60} (B) NP-aq spectra, (C) NP-oil spectra, (D) Ni K-edge oxidation numbers from literature, ^{11, 51, 60-61} (E) NP-aq spectra, and (F) NP-oil spectra. Note: reference material comparisons were also measured by the authors.

4.6 Operando EXAFS Analysis

An analysis EXAFS of spectra at the Fe K-edge for both NP-aq and NP-oil electrocatalysts provides structural insight into the transitions occurring in the catalysts during the chronoamperometry experiment. The best fits of the EXAFS data on the Fourier-transformed (FT) spectra of the key voltages are shown in Figure 8, and the resulting wavelet transforms are shown in Figure S9. All of the EXAFS fitting parameters related to Figure 8 are presented in Tables S1 – S4 and the corresponding fits are shown in Figure S10. Full sets of EXAFS FT spectra are shown in Figure S11 – S12, with fits shown in Figure S13 – S20 and tabulated fitting parameters reported in Tables S5 – S11. The first peak in the FT, cursorily assigned to a metal-oxygen scattering path, of the spectra for the NP-aq Fe K-edge during the anodic ramp (Figure 8A and Figure S11A) converts from a broad peak at the initial voltage of 0.0 V vs. Ag/AgCl to a peak with a distinct shoulder above 0.7 V vs. Ag/AgCl, with a distinct smaller peak feature at ~1.9 Å. All spectra also show a peak feature at just above 1.0 Å. This broad peak feature that is observed during both the anodic ramp and the cathodic ramp (with subtle peak splitting apparent at the 0.1 V cathodic step) suggests the presence of two unique Fe – O species. Qualitative analysis of the EXAFS spectra for the NP-aq catalyst also suggests a compression of the Fe – O bond distance when the voltage is stepped from 0.7 V to 0.8 V vs. Ag/AgCl on the anodic voltage ramp. The second peak in the FT, assigned to metal-metal (Fe – M) bond distances, is also shortened during the anodic ramp, as can be seen in the peak shift to smaller radial distance (i.e., for the peak located between 2 and 3 Å). In the case of the cathodic ramp (Figure S11B), the NP-aq start a transformation between 0.7 V and 0.6 V vs. Ag/AgCl, assumed to be the reversible transition back to the initial phase, with the elongation of the metal-metal bond length and the broadening of the metal-oxygen bond.

During the anodic ramp for NP-oil Fe K-edge (Figure 8B and Figure S11C), a decrease in metal-oxygen and metal-metal bond lengths can be observed. However, for the NP-oil, the decrease in bond lengths does not occur until the voltage step from 0.8 V to 0.9 V vs. Ag/AgCl. In both anodic and cathodic ramps for NP-oil (Figure S11C, D), the metal-oxygen peak shape remains largely unchanged, and the metal-metal peak shifts back to its original position after 0.6 V vs. Ag/AgCl. The Fe – M peak region in the NP-oil contains a single peak until 0.8 V vs. Ag/AgCl, where two peaks are clearly observed. These two peaks are suggestive of Fe species existing in multiple coordination environments, similar spectrally to that of a maghemite structure (i.e., Fe₂O₃), 62 as well as substituted into α -Ni(OH)₂.

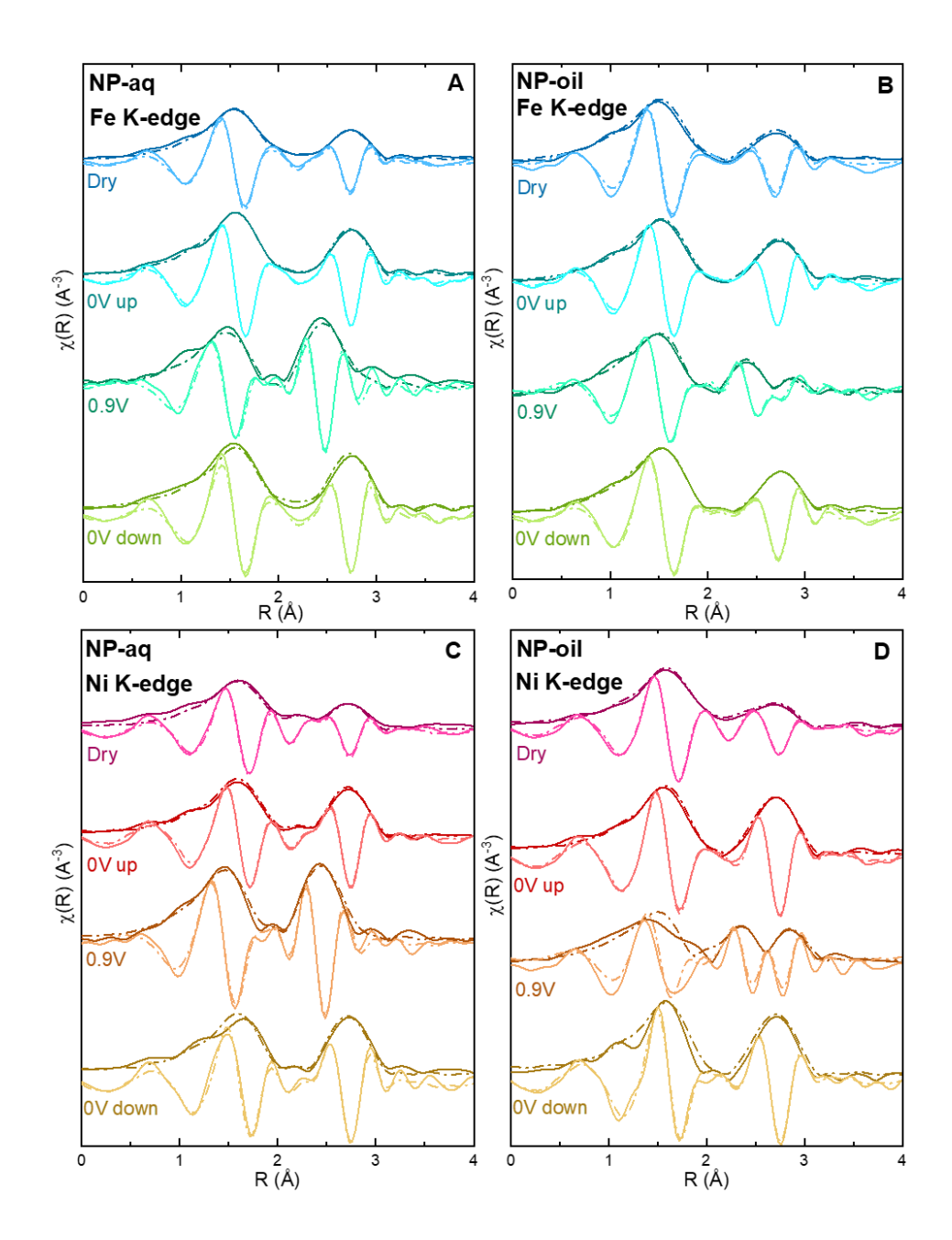


Figure 8. Experimental EXAFS spectra at the Fe K-edge and Ni K-edge for NP-aq and NP-oil nanoparticles are shown as solid lines. The real component is shown in darker color, and the imaginary component is shown in lighter color for each sample. Fits are shown in dashed lines for (A) NP-aq Fe K-edge, (B) NP-oil Fe K-edge, (C) NP-aq Ni K-edge, and (D) NP-oil Ni K-edge. All experiments were performed in purified 1.0 M KOH (pH 14), and all voltages are reported as measured vs. Ag/AgCl (3 M NaCl) reference electrode.

The splitting of the Fe - O peak has been reported in other FeNiO(H)_x materials (e.g., NiFe₂O₄ ferrite materials^{15, 63}) and iron oxides, ^{62, 64-65} but not in sister FeMO_x materials (e.g., CoFe₂O₄, ¹⁵ CoFe(OH)_x⁶⁶), suggesting that the nanoparticle synthesis and subsequent electrochemical environment cause two unique Fe - O species in FeNiO_x-type materials, in particular. Interestingly, studies on FeNi layered double hydroxides, including electrodeposited FeNi hydroxide films, do not result in a particularly broad Fe - O peak feature or a doublet splitting of the Fe - O peak, ^{11, 16, 27} suggesting that the as-synthesized structure and possibly even the synthesis route can affect the operando catalytic structure of these similar FeNiO(H)_x materials. Since the majority of operando XAS studies thus far on FeNiO(H)_x materials have primarily focused on electrodeposited FeNi hydroxide films, there remains a significant knowledge gap as to how and if other related FeNiO(H)_x electrocatalyst morphologies have similar or different atomic-scale operando structures.

The Fe – O bond distance fitted from the EXAFS for the as-synthesized dry sample for NP-aq was found to be 2.00 Å (Table S1 and Figure 9). The Fe – O bond distance identified in the assynthesized dry sample aligns with the average reported Fe(III) – O distance of 2.02 Å (from two separate bond lengths of 1.95 and 2.09 Å) reported for α -FeOOH^{53,67-68} and an Fe(III) – O distance of 1.99 – 2.00 Å reported for γ -FeOOH,^{53,67} supporting the selection of γ -FeOOH as the structural model for EXAFS data analysis. The bond distances remain within 0.1 Å for all three scattering paths at both 0.0 V at the start of the anodic ramp and 0.0 V at the completion of the cathodic ramp but show a slight compression of the Fe – O bond distance to 1.91 Å at 0.8 V – 0.9 V vs. Ag/AgCl (1.82 V – 1.92 V vs. RHE). In comparison, Friebel et al. ¹¹ studied electrodeposited FeNi hydroxide films and reported an Fe – O bond distance of 2.01 - 2.05 Å at low voltages, but a compression of the Fe – O bond distance to 1.89 Å at 1.62 V vs. RHE. Similarly, Gonzalez-Flores et al. ²⁷ found

an initial Fe – O distance of 2.05 Å and a compressed Fe – O atomic pair of 1.92 Å at 1.55 V vs. RHE.

While perhaps not obvious from the EXAFS spectra in Figures 8 and S10, the best fit model for the Fe $-M_x$ peaks in the NP-aq was consistent with two distinct metal - metal scattering paths at 2.54 Å and 3.11 Å, respectively, at 0.0 V vs. Ag/AgCl. These two Fe – M_x atomic pair distances shift to 2.50 Å and 2.86 Å after the anodic ramp to 0.9 V vs. Ag/AgCl but revert to 2.54 Å and $3.12~\mbox{Å}$ after the cathodic ramp to $0.0~\mbox{V}$. The smaller Fe $-\,\mbox{M}_1$ atomic pair distance of $2.54~\mbox{Å}$ at $0.0~\mbox{M}_2$ V is consistent with a metal – metal bond length for Fe – Fe, 27 while Fe – M_2 at 0.0 V aligns with other Fe-incorporated Ni(OH)₂ materials such as those reported by Friebel et al., ¹¹ suggesting that the Fe species represented by this atom pair is likely in a chemical environment where it is substituted for Ni in α-Ni(OH)₂. The compression of Fe – M₂ at 0.9 V vs. Ag/AgCl to 2.86 Å is similar to that observed for Fe – Ni (2.85 Å) and Ni – Ni (2.86 Å) shortened bonds reported by Gonzalez-Flores et al.²⁷ at 1.55 V vs. RHE, as well as Fe – Ni (2.84 Å) and Ni-Ni (2.82 Å) atomic pairs at 1.62 V vs. RHE reported by Friebel et al. 11 This result for Fe – M2 at 0.9 V suggests again that this Fe species is substituted for Ni in the γ -NiOOH phase that forms under applied potential.¹¹ The results for Fe – M₁ indicate that the metallic component of the NP-ag²⁰ formed during our synthesis process is retained during electrochemical treatment.

NP-oil at the Fe K-edge was fitted using four scattering paths (Fe – O, Fe – M_1 , Fe – M_2 , and Fe – M_3). We note that both NP-aq and NP-oil were modeled using one, two, or three Fe- M_x scattering paths, and the result was that NP-aq was best fit with only two Fe- M_x paths, while NP-oil was best fit with three Fe- M_x paths. A discussion of this difference follows below. The bond distances for the sample at 0.0 V vs. Ag/AgCl before the anodic ramp and after the cathodic ramp remained within 0.1 Å for Fe – O, Fe – M_2 , and Fe – M_3 , but shortened by 0.04 Å for the Fe – M_1 path (Table

S2 and Figure 9). At 0.0 V vs. Ag/AgCl, the Fe – O atomic pair distance is estimated at 2.00 Å, with a slight compression to 1.96 Å at 0.9 V. The Fe – M_2 and Fe – M_3 atomic pair distances are estimated at 2.99 Å and 3.12 Å at 0.0 V vs. Ag/AgCl, shifting to 2.87 Å and 3.06 Å at 0.9 V; the data were successfully modeled with only two Fe – M_x scattering paths at 0.9 V (Table S7). These results for NP-oil suggest a different chemical environment for the Fe species, as compared to the results for the NP-aq. The core-shell structure of NP-oil likely contributed to Fe species being in two distinct phases at bond distances around 3 ± 0.15 Å. The Fe – O atomic pair distance at 0.0 V is shorter than what might be expected for a phase where Fe is incorporated as a substitute for Ni in a nominally α -Ni(OH)₂ phase. In addition, the change in Fe – O at 0.9 V is less drastic for NP-oil vs. NP-aq. Taken together, the Fe – O and Fe – M_x atomic pair distances of the NP-oil suggest that a large portion of the Fe species is in a maghemite-like phase (i.e., γ -Fe₂O₃), ^{62, 64-65} which has Fe – O and Fe – Fe atomic pair distances at 1.97 Å (for a single path model)⁶⁵ and 2.99 Å, ⁶⁴ with a portion of the Fe species in NP-oil likely incorporated into α -Ni(OH)₂. ¹¹

Both NP-aq and NP-oil result in a decrease in the coordination number (CN) for the Fe species at 0.9 V vs. Ag/AgCl (1.92 V vs. RHE). For the NP-aq electrocatalyst, the lower CN of 4.5 suggests a transition to tetrahedral geometry, a conclusion which is supported by the Fe K-pre-edge analysis. In contrast, the NP-oil electrocatalyst results in a CN of 5.3 at 0.9 V vs. Ag/AgCl, which could suggest some portion of the Fe species transitions to a tetrahedral coordination environment, similar to what was observed by Friebel et al.;¹¹ however, our Fe K-pre-edge results in Figure 4 suggest the Fe species is largely in the octahedral coordination environment. This difference in the Fe structural environment between the two NP electrocatalyst materials is possibly a key to the differences observed in the OER activity and stability and points to differences in NP structure obtained through two different synthesis routes. In particular, the NP-oil synthesis route is based

on the initial formation of an NiO_x core nanoparticle, with subsequent formation of a FeO_x shell that becomes a FeNiO_x shell as a result of Ni migration from the core into the shell. As reported in our prior work, ²⁵ the elevated temperature of the FeO_x shell formation step (220 °C) likely enabled Ni migration and the integration of a bimetallic oxide phase during shell formation. NP-oil synthesis occurs more slowly and results in an oxide-oxide core-shell structure, while the NP-aq synthesis occurs through fast nucleation and growth via a BH₄-induced reduction reaction of both Fe and Ni salt precursors. The reduction reaction approach results in a more disordered, heterogeneous particulate morphology and a metal core-hydroxide shell. ²⁰ Both the core and the shell are bimetallic, containing both Fe and Ni species, and the shell has been characterized to consist of a disordered Ni(OH)₂-like chemical structure. ²⁰ While both NP materials result in quite similar Ni chemistry under operando conditions (described in detail below), the key differences, i.e., the Fe O_h \rightarrow T_d transition in NP-aq, the presence of Fe and Ni metallic species in NP-aq, and the presence of a separate maghemite-like phase in NP-oil are directly correlated to the synthesis route and the resulting OER performance metrics.

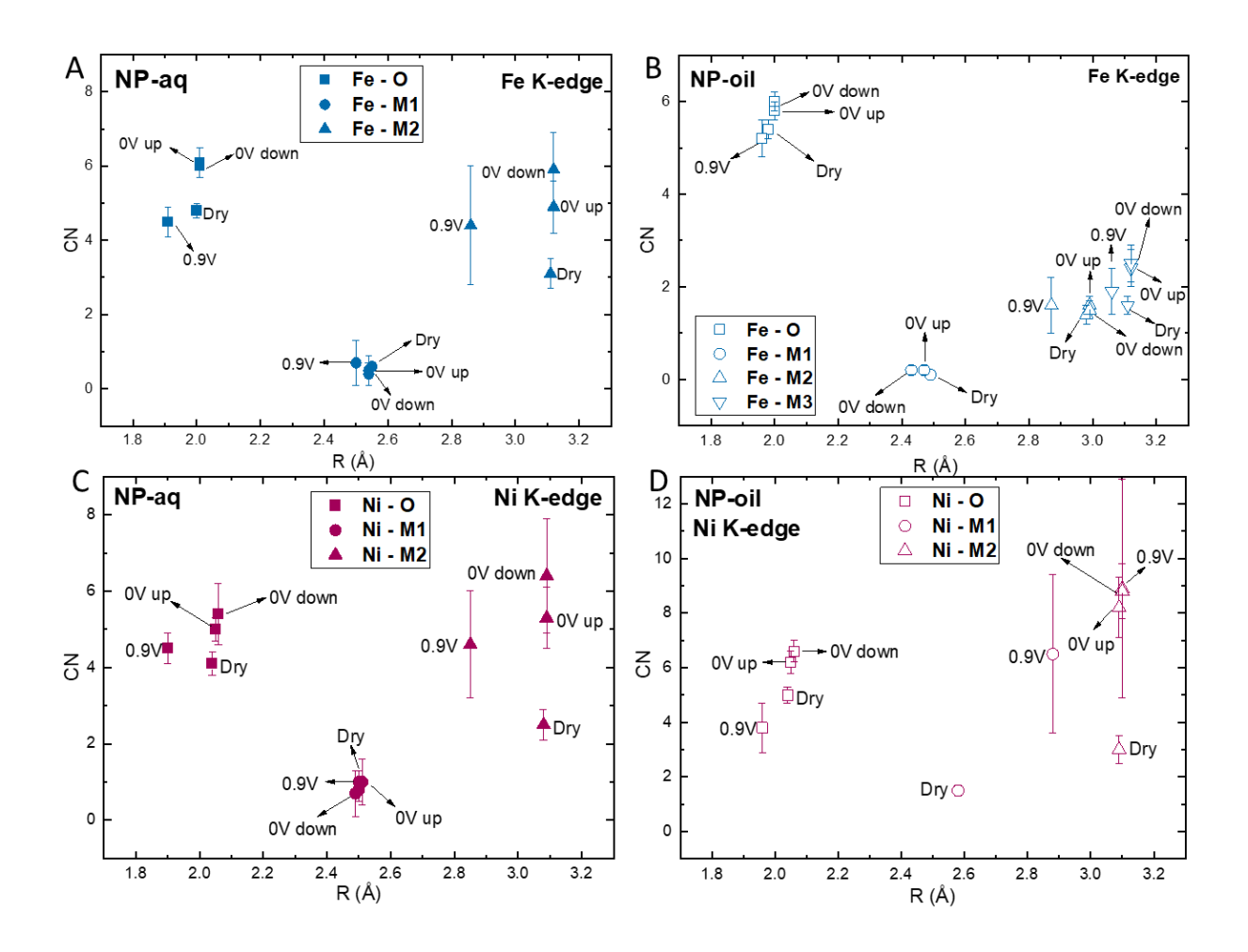


Figure 9. Coordination number (CN) vs. bond distance (R) obtained from the EXAFS fits of: (A) Fe K-edge for NP-aq, (B) NP-oil (B), and (C) Ni K-edge spectra for NP-aq, (D) NP-oil.

EXAFS spectra at the Ni K-edge for both NP-aq and NP-oil show significant changes in the atomic chemistry of the catalysts during the potential hold experiment as shown in Figures 8C, D and S12. During the anodic ramp for NP-aq (Figure S12A), the spectral shape is largely maintained until 0.8 V vs. Ag/AgCl, when both the metal – oxygen and metal – metal atomic pair distances shorten. During the cathodic ramp (Figure S12B), the NP-aq nanoparticle catalyst appears to transform back into the initial phase. For NP-oil (Figures 9D and S12), significant variation in the spectral

shape can be observed. At the highest voltage of 0.9 V vs. Ag/AgCl, the metal – metal path splits into two distinct components. On the cathodic ramp (Figure S12D), the two metal-metal paths recombine at 0.6 V, where the spectrum reverts to a spectral shape similar to its initial state.

The Ni – O bond distance fitted from the EXAFS spectra for the as-synthesized dry NP-aq sample was found to be 2.04 Å (Table S3, Figure 9, and Figure S6), and at both 0.0 V vs. Ag/AgCl potential steps, the Ni – O bond distance remains essentially unchanged at 2.05 – 2.06 Å. However, at 0.9 V vs. Ag/AgCl, the Ni – O bond distance is shortened to 1.90 Å much like the shortening of the Fe – O bond length observed for NP-aq under applied voltage. These modeling results align with those reported by Gonzalez-Flores et al.²⁷ and Friebel et al.,¹¹ who both reported that at voltages below the onset of the OER, the Ni – O atomic pair distance is estimated at 2.05 – 2.06 Å, characteristic of α-Ni(OH)₂.⁶⁹⁻⁷⁰ Further, under voltages within the Faradaic OER regime (i.e., $1.62~V~vs.~RHE~for~Friebel~et~al., ^{11}~1.55~V~vs.~RHE~for~Gonzalez-Flores~et~al., ^{27}~and~1.6-1.9~V~vs.$ vs. RHE for this study), a compression of the Ni – O atomic pair distance to 1.89 - 1.90 Å is consistently observed. In addition, the nickel-metal peaks (Ni – M_x) of the NP-aq for the dry sample and the sample in the electrochemical environment at 0.0 V vs. Ag/AgCl are 2.50 – 2.51 Å and 3.08 - 3.09 Å, with a decrease in Ni – M₂ to 2.85 Å at 0.9 V, while Ni – M₁ remains stable at 2.51 Å. The Ni – M₁ bond length at 2.50 Å matches with the expected Ni – Ni metal atom pair distance, ^{27, 71} and the presence of this atom pair distance throughout the voltage ramps suggests that the NP-ag retain a metallic component, which we previously identified to exist in the core of these catalysts, ²⁰ while the shell mixed FeNi hydroxide phase transitions between hydroxide (3.08 $-3.09 \text{ Å})^{69}$ and oxyhydroxide (2.85 Å) as a function of voltage. The Ni – M₂ atomic pair distance for our and other Fe-incorporated Ni(OH)₂ materials is smaller than that of pure Ni(OH)₂, reported at $3.16~\text{Å}.^{70}$ The compression of the Ni-M₂ atomic pair distance aligns with the expected distance

in Fe-incorporated γ-NiOOH (e.g., 2.82 Å reported for Fe₂₅Ni₇₅OOH films at 1.62 V vs. RHE by Friebel et al.¹¹ and 2.86 Å reported for Fe₄₀Ni₆₀OOH films at 1.55 V vs. RHE by Gonzalez-Flores et al.²⁷).

These results suggest that for Ni species in the NP-aq catalyst, the primary chemical environment of the electrochemically-active component in the as-synthesized, low-voltage, and OER Faradaic voltage conditions is that of the α-Ni(OH)₂/γ-NiOOH redox pair, with the core metal component of the as-synthesized nanoparticles retained during anodic/cathodic ramps. In this aspect of the chemical structure of the NP-aq catalyst, both the nanoparticles and the electrodeposited films of Gonzalez-Flores et al.²⁷ and Friebel et al.¹¹ appear to have structurally similar Ni species that are in a hydroxide phase, and this similarity is in contrast to the Fe chemical environment of the NP-aq, which seem to be dissimilar to the electrodeposited films. This result also shows that with careful analysis of the operando XAS data, along with knowledge of the as-synthesized nanoparticle morphology and structure, it is possible to use this nominally bulk characterization technique to capture chemical changes that occur for the electrochemically active portion of the metal species that may be at or near the surface of the electrocatalyst.

For NP-oil, under dry and 0.0 V vs. Ag/AgCl conditions, the Ni – O atom pair distance remains consistently at 2.04 Å – 2.06 Å, again characteristic of α -Ni(OH)₂. When the 0.9 V vs. Ag/AgCl potential is applied, a shorter Ni – O distance of 1.90 Å is observed, indicative of γ -NiOOH. In addition, the nickel metal-metal peak (Ni – M) between 2 and 3 Å also splits into a doublet at higher voltages, and this doublet is maintained in the cathodic ramp until 0.7 V vs. Ag/AgCl. Ni – M_x atomic pair distances are estimated at 2.58 Å and 3.09 Å for as prepared dry nanoparticles (Figure 9 and Table S4). At 0.0 V vs. Ag/AgCl at the beginning of the anodic voltage ramp, the metal component disappears while Ni – M_2 remains at 3.09 Å. At 0.9 V vs. Ag/AgCl, Ni – M_x

shift to 2.88 Å and 3.10 Å. Finally, after the cathodic ramp to 0.0 V vs. Ag/AgCl, the second Ni – M_x peak disappears, similar to that of anodic ramp at same potential. These results for the Ni – M_x peaks suggest that the as-synthesized material contains both Ni metal and Ni(OH)₂ chemical environments, shifting to a mix of hydroxide and oxyhydroxide phases under voltage, and converting to a fully oxidized material post voltage ramp (i.e., the Ni metal component of the Ni atoms is not retained post-electrochemical treatment). The two different Ni – M_x atomic pair distances are indicative of a Fe-incorporated α -Ni(OH)₂ phase^{11,72} and a pure Ni(OH)₂ phase,^{70,72} likely as the shell and the core, respectively, of the nanoparticle catalyst, where the shell of Fe-incorporated α -Ni(OH)₂ is shifting between the α -Ni(OH)₂/ γ -NiOOH redox pair. Again, these results indicate that operando XAS measurements can in fact be used to interpret changes in nanoparticle materials that do have a complex bulk three-dimensional morphology, but that care must be taken to understand the three-dimensional structure and appropriately interpret the XAS results with knowledge of the as-synthesized structure.

5. Conclusions

In this work, we investigated the behavior of two nanoparticle electrocatalysts, synthesized via aqueous and solvothermal solution phase approaches, during OER conditions using operando XAS. Our results show that the chemical changes of the two nanoparticles have similarities and differences under OER Faradaic voltages and as a result of anodic and cathodic voltage ramps. The nanoparticles synthesized via aqueous phase solution chemistry (NP-aq) resulted in Fe species that transitioned between Fe³⁺ T_d and Fe³⁺ O_h with applied voltage, while the solvothermally synthesized nanoparticles (NP-oil) remained largely in a Fe³⁺ O_h coordination environment, albeit with some level of structural disorder. An analysis of the EXAFS regions of both Fe K-edge and

Ni K-edge showed that the NP-aq have Fe species that transition reversibly to compressed Fe – O and Fe – M_x atomic pair distances. However, the Fe species in NP-oil appear to exist in multiple phases, with three (rather than two) Fe – M_x scattering paths fit to the data. Both nanoparticle types resulted in Fe – O peak shapes that were broad and included a shoulder at smaller radial distance, suggesting multiple Fe – O scattering paths. NP-aq showed evidence of metallic Fe and Ni, which appear to be retained under applied OER voltages; in contrast, the metallic Ni component of the NP-oil appears to be irreversibly oxidized after voltage was applied, and there was no evidence of metallic Fe in the NP-oil. Both nanoparticle types showed reversible Ni – O and Ni – M_x atomic pair compressions at OER voltages, with Ni largely existing as hydroxide/oxyhydroxide. XANES edge analyses suggest that a qualitative rather than a quantitative approach needs to be taken while establishing a relationship between oxidation state and the edge energy position as the coordination environment and the structural changes could be playing equal if not greater roles during the OER electrocatalysis. However, the Fe K-edge pre-edge can be analyzed to understand coordination environment and oxidation state changes. The subtle differences in atomic structure between the two nanoparticle electrocatalysts are correlated to the synthesis route and observed differences in OER performance. In particular, it appears that an Fe species transition from O_h to T_d, along with a majority Fe-incorporated Ni(OH)₂-like phase in the shell and a metallic core contribute to the improved OER performance of the NP-aq sample, including both OER activity and stability. Given the dearth of operando XAS studies on nanoparticle electrocatalysts that have been performed at high enough voltages to observe such structural changes, these results point to the importance of further studies on FeNiO(H)_x nanoparticles that continue to delineate the roles of morphology and synthesis route on operando structure, and how operando structure is correlated to performance metrics.

Acknowledgements

Use of the Stanford Synchrotron Radiation Lightsource, SLAC National Accelerator Laboratory is supported by the U.S. Department of Energy, Office of Basic Energy Sciences under Contract No. DE-AC02-76SF00515. Co-ACCESS is supported by the U.S. Department of Energy, Office of Science, Office of Basic Energy Sciences, Chemical Sciences, Geosciences, and Biosciences Division. LFG, PA, JC, and RM acknowledge support from the National Science Foundation under award number 1703827. LFG and PA also acknowledge support from the University of Arkansas for travel funds related to synchrotron beam time experimental trips.

Supporting Information. The following materials are supplied in the Supporting Information file:

- Design schematics of the operando electrochemical cell
- Additional characterization data for the nanoparticles
- XANES spectra of the dry nanoparticle samples
- LCF results
- Continuous Cauchy wavelet transforms of Fe and Ni K-edge EXAFS
- EXAFS experimental data and modeling fits
- Modeling fit parameters of EXAFS analysis

References

- 1. Burke, M. S.; Enman, L. J.; Batchellor, A. S.; Zou, S.; Boettcher, S. W., Oxygen Evolution Reaction Electrocatalysis on Transition Metal Oxides and (Oxy)Hydroxides: Activity Trends and Design Principles. *Chem. Mater.* **2015**, 27, 7549-7558.
- 2. Trotochaud, L.; Boettcher, S. W., Precise Oxygen Evolution Catalysts: Status and Opportunities. *Scripta Mater.* **2014**, 74, 25-32.
- 3. Grimaud, A.; Diaz-Morales, O.; Han, B.; Hong, W. T.; Lee, Y.-L.; Giordano, L.; Stoerzinger, K. A.; Koper, M. T.; Shao-Horn, Y., Activating Lattice Oxygen Redox Reactions in Metal Oxides to Catalyse Oxygen Evolution. *Nat. Chem.* **2017**, 9, 457-465.
- 4. McCrory, C. C.; Jung, S.; Peters, J. C.; Jaramillo, T. F., Benchmarking Heterogeneous Electrocatalysts for the Oxygen Evolution Reaction. *J. Am. Chem. Soc.* **2013**, 135, 16977-16987.
- 5. Xiao, H.; Shin, H.; Goddard, W. A., Synergy between Fe and Ni in the Optimal Performance of (Ni,Fe)Ooh Catalysts for the Oxygen Evolution Reaction. *Proc. National Acad. Sci.* **2018**, 115, 5872-5877.
- 6. Martirez, J. M. P.; Carter, E. A., Unraveling Oxygen Evolution on Iron-Doped B-Nickel Oxyhydroxide: The Key Role of Highly Active Molecular-Like Sites. *J. Am. Chem. Soc.* **2019**, 141, 693-705.
- 7. Trotochaud, L.; Young, S. L.; Ranney, J. K.; Boettcher, S. W., Nickel-Iron Oxyhydroxide Oxygen-Evolution Electrocatalysts: The Role of Intentional and Incidental Iron Incorporation. *J. Am. Chem. Soc.* **2014**, 136, 6744-6753.

- 8. Burke, M. S.; Zou, S.; Enman, L. J.; Kellon, J. E.; Gabor, C. A.; Pledger, E.; Boettcher, S. W., Revised Oxygen Evolution Reaction Activity Trends for First-Row Transition-Metal (Oxy)Hydroxides in Alkaline Media. *J. Phys. Chem. Lett.* **2015**, 6, 3737-3742.
- 9. Corrigan, D. A.; Bendert, R. M., Effect of Coprecipitated Metal Ions on the Electrochemistry of Nickel Hydroxide Thin Films: Cyclic Voltammetry in 1m Koh. *J. Electrochem. Soc.* **1989**, 136, 723-728.
- 10. Corrigan, D. A., The Catalysis of the Oxygen Evolution Reaction by Iron Impurities in Thin Film Nickel Oxide Electrodes. *J. Electrochem. Soc.* **1987**, 134, 377-384.
- 11. Friebel, D.; Louie, M. W.; Bajdich, M.; Sanwald, K. E.; Cai, Y.; Wise, A. M.; Cheng, M.-J.; Sokaras, D.; Weng, T.-C.; Alonso-Mori, R.; Davis, R. C.; Bargar, J. R.; Nørskov, J. K.; Nilsson, A.; Bell, A. T., Identification of Highly Active Fe Sites in (Ni,Fe)Ooh for Electrocatalytic Water Splitting. *J. Am. Chem. Soc.* **2015**, 137, 1305-1313.
- 12. Abbott, D. F.; Fabbri, E.; Borlaf, M.; Bozza, F.; Schäublin, R.; Nachtegaal, M.; Graule, T.; Schmidt, T. J., Operando X-Ray Absorption Investigations into the Role of Fe in the Electrochemical Stability and Oxygen Evolution Activity of Ni_{1-X}fe_xo_y Nanoparticles. *J. Mater. Chem. A* **2018**, 6, 24534-24549.
- 13. Lee, H. J.; Back, S.; Lee, J. H.; Choi, S. H.; Jung, Y.; Choi, J. W., Mixed Transition Metal Oxide with Vacancy-Induced Lattice Distortion for Enhanced Catalytic Activity of Oxygen Evolution Reaction. *ACS Catal.* **2019**, 9, 7099-7108.

- 14. Bau, J. A.; Luber, E. J.; Buriak, J. M., Oxygen Evolution Catalyzed by Nickel–Iron Oxide Nanocrystals with a Nonequilibrium Phase. *ACS Appl. Mater. Inter.* **2015**, 7, 19755-19763.
- 15. Balachandran, G.; Dixon, D.; Bramnik, N.; Bhaskar, A.; Yavuz, M.; Pfaffmann, L.; Scheiba, F.; Mangold, S.; Ehrenberg, H., Elucidation of the Electrochemical Reaction Mechanism in Mfe2o4 (M=Ni, Co) Conversion-Type Negative Electrode Systems by Using in Situ X-Ray Absorption Spectroscopy. *ChemElectroChem* **2015**, 2, 1510-1518.
- 16. Cai, Z.; Zhou, D.; Wang, M.; Bak, S.-M.; Wu, Y.; Wu, Z.; Tian, Y.; Xiong, X.; Li, Y.; Liu, W.; Siahrostami, S.; Kuang, Y.; Yang, X.-Q.; Duan, H.; Feng, Z.; Wang, H.; Sun, X., Introducing Fe²⁺ into Nickel–Iron Layered Double Hydroxide: Local Structure Modulated Water Oxidation Activity. *Angew. Chem.* **2018**, 130, 9536-9540.
- 17. Dionigi, F.; Zeng, Z.; Sinev, I.; Merzdorf, T.; Deshpande, S.; Lopez, M. B.; Kunze, S.; Zegkinoglou, I.; Sarodnik, H.; Fan, D.; Bergmann, A.; Drnec, J.; Araujo, J. F. d.; Gliech, M.; Teschner, D.; Zhu, J.; Li, W.-X.; Greeley, J.; Cuenya, B. R.; Strasser, P., In-Situ Structure and Catalytic Mechanism of Nife and Cofe Layered Double Hydroxides During Oxygen Evolution. *Nat. Commun.* **2020**, 11, 2522.
- 18. Chen, G.; Zhu, Y.; Chen, H. M.; Hu, Z.; Hung, S.-F.; Ma, N.; Dai, J.; Lin, H.-J.; Chen, C.-T.; Zhou, W.; Shao, Z., An Amorphous Nickel–Iron-Based Electrocatalyst with Unusual Local Structures for Ultrafast Oxygen Evolution Reaction. *Adv. Mater.* **2019**, 31, 1900883.

- 19. Fu, S.; Song, J.; Zhu, C.; Xu, G.-L.; Amine, K.; Sun, C.; Li, X.; Engelhard, M. H.; Du, D.; Lin, Y., Ultrafine and Highly Disordered Ni₂fe₁ Nanofoams Enabled Highly Efficient Oxygen Evolution Reaction in Alkaline Electrolyte. *Nano Energy* **2018**, 44, 319-326.
- 20. Acharya, P.; Nelson, Z. J.; Benamara, M.; Manso, R. H.; Bakovic, S. I. P.; Abolhassani, M.; Lee, S.; Reinhart, B.; Chen, J.; Greenlee, L. F., Chemical Structure of Fe–Ni Nanoparticles for Efficient Oxygen Evolution Reaction Electrocatalysis. *ACS Omega* **2019**, 4, 17209-17222.
- 21. Görlin, M.; Chernev, P.; Paciok, P.; Tai, C.-W.; de Araújo, J. F.; Reier, T.; Heggen, M.; Dunin-Borkowski, R.; Strasser, P.; Dau, H., Formation of Unexpectedly Active Ni–Fe Oxygen Evolution Electrocatalysts by Physically Mixing Ni and Fe Oxyhydroxides. *Chem. Commun.* **2019**, 55, 818-821.
- 22. Tao, J.; Zhang, Y.; Wang, S.; Wang, G.; Hu, F.; Yan, X.; Hao, L.; Zuo, Z.; Yang, X., Activating Three-Dimensional Networks of Fe@Ni Nanofibers Via Fast Surface Modification for Efficient Overall Water Splitting. *ACS Appl. Mater. Interfacec* **2019**, 11, 18342–18348.
- 23. Wu, G.; Chen, W.; Zheng, X.; He, D.; Luo, Y.; Wang, X.; Yang, J.; Wu, Y.; Yan, W.; Zhuang, Z.; Hong, X.; Li, Y., Hierarchical Fe-Doped Niox Nanotubes Assembled from Ultrathin Nanosheets Containing Trivalent Nickel for Oxygen Evolution Reaction. *Nano Energy* **2017**, 38, 167-174.
- 24. Moghimi, N.; Abdellah, M.; Thomas, J. P.; Mohapatra, M.; Leung, K. T., Bimetallic Feni Concave Nanocubes and Nanocages. *J. Am. Chem. Soc.* **2013**, 135, 10958-10961.
- 25. Manso, R. H.; Acharya, P.; Deng, S.; Crane, C. C.; Reinhart, B.; Lee, S.; Tong, X.; Nykypanchuk, D.; Zhu, J.; Zhu, Y.; Greenlee, L. F.; Chen, J., Controlling the 3-D Morphology

- of Ni–Fe-Based Nanocatalysts for the Oxygen Evolution Reaction. *Nanoscale* **2019**, 11, 8170-8184.
- 26. Candelaria, S. L.; Bedford, N. M.; Woehl, T. J.; Rentz, N. S.; Showalter, A. R.; Pylypenko, S.; Bunker, B. A.; Lee, S.; Reinhart, B.; Ren, Y.; Ertem, S. P.; Coughlin, E. B.; Sather, N. A.; Horan, J. L.; Herring, A. M.; Greenlee, L. F., Multi-Component Fe–Ni Hydroxide Nanocatalyst for Oxygen Evolution and Methanol Oxidation Reactions under Alkaline Conditions. *ACS Catal.* **2017**, 7, 365-379.
- 27. González-Flores, D.; Klingan, K.; Chernev, P.; Loos, S.; Mohammadi, M. R.; Pasquini, C.; Kubella, P.; Zaharieva, I.; Smith, R. D.; Dau, H., Nickel-Iron Catalysts for Electrochemical Water Oxidation–Redox Synergism Investigated by in Situ X-Ray Spectroscopy with Millisecond Time Resolution. *Sustain. Energy Fuels* **2018**, 2, 1986-1994.
- 28. Stevens, M. B.; Trang, C. D. M.; Enman, L. J.; Deng, J.; Boettcher, S. W., Reactive Fe-Sites in Ni/Fe (Oxy)Hydroxide Are Responsible for Exceptional Oxygen Electrocatalysis Activity. *J. Am. Chem. Soc.* **2017**, 139, 11361-11364.
- 29. Song, F.; Busch, M. M.; Lassalle-Kaiser, B.; Hsu, C.-S.; Petkucheva, E.; Bensimon, M.; Chen, H. M.; Corminboeuf, C.; Hu, X., An Unconventional Iron Nickel Catalyst for the Oxygen Evolution Reaction. *ACS Cent. Sci.* **2019**, *5*, 558-568.
- 30. Görlin, M.; Ferreira de Araújo, J.; Schmies, H.; Bernsmeier, D.; Dresp, S.; Gliech, M.; Jusys, Z.; Chernev, P.; Kraehnert, R.; Dau, H.; Strasser, P., Tracking Catalyst Redox States and Reaction Dynamics in Ni–Fe Oxyhydroxide Oxygen Evolution Reaction Electrocatalysts: The Role of Catalyst Support and Electrolyte Ph. *J. Am. Chem. Soc.* **2017**, 139, 2070-2082.

- 31. Görlin, M.; Chernev, P.; Ferreira de Araújo, J.; Reier, T.; Dresp, S.; Paul, B.; Krähnert, R.; Dau, H.; Strasser, P., Oxygen Evolution Reaction Dynamics, Faradaic Charge Efficiency, and the Active Metal Redox States of Ni–Fe Oxide Water Splitting Electrocatalysts. *J. Am. Chem. Soc.* **2016**, 138, 5603-5614.
- 32. Boubnov, A.; Lichtenberg, H.; Mangold, S.; Grunwaldt, J.-D., Identification of the Iron Oxidation State and Coordination Geometry in Iron Oxide- and Zeolite-Based Catalysts Using Pre-Edge Xas Analysis. *J. Synch. Rad.* **2015**, 22, 410-426.
- 33. Roe, A.; Schneider, D.; Mayer, R.; Pyrz, J.; Widom, J.; Que Jr, L., X-Ray Absorption Spectroscopy of Iron-Tyrosinate Proteins. *J. Am. Chem. Soc.* **1984**, 106, 1676-1681.
- 34. Shadle, S. E.; Hedman, B.; Hodgson, K. O.; Solomon, E. I., Ligand K-Edge X-Ray Absorption Spectroscopic Studies: Metal-Ligand Covalency in a Series of Transition Metal Tetrachlorides. *J. Am. Chem. Soc.* **1995**, 117, 2259-2272.
- 35. Vračar, M.; Kuzmin, A.; Merkle, R.; Purans, J.; Kotomin, E. A.; Maier, J.; Mathon, O., Jahn-Teller Distortion around Fe⁴⁺ in Sr(Fe_xti_{1-X})O_{3-Δ} from X-Ray Absorptionspectroscopy, X-Ray Diffraction, and Vibrational Spectroscopy. *Phys. Rev. B* **2007**, 76, 174107.
- 36. Westre, T. E.; Kennepohl, P.; DeWitt, J. G.; Hedman, B.; Hodgson, K. O.; Solomon, E. I., A Multiplet Analysis of Fe K-Edge 1s → 3d Pre-Edge Features of Iron Complexes. *J. Am. Chem. Soc.* **1997**, 119, 6297-6314.
- 37. Wilke, M.; Farges, F. o.; Petit, P.-E.; Brown, G. E., Jr.; Martin, F. o., Oxidation State and Coordination of Fe in Minerals: An Fe K-Xanes Spectroscopic Study. *Am. Mineral.* **2001**, 86, 714-730.

- 38. Acharya, P.; Burrow, J.; Abolhassani, M.; Greenlee, L. F., Role of Surface Area on the Performance of Iron Nickel Nanoparticles for the Oxygen Evolution Reaction (Oer). *ECS Trans*. **2018**, 85, 81-89.
- 39. Greenlee, L. F.; Acharya, P.; Nelson, Z., Compositional Optimization of Alloy Fe_xni_y(Oh)₂ Nanoparticles for Alkaline Electrochemical Oxygen Evolution. *ECS Trans.* **2017**, 77, 25-38.
- 40. Ravel, B.; Newville, M., Athena, Artemis, Hephaestus: Data Analysis for X-Ray Absorption Spectroscopy Using Ifeffit. *J. Synchrotron Rad.* **2005**, 12, 537-541.
- 41. Newville, M., Larch: An Analysis Package for Xafs and Related Spectroscopies. **2013**, 430, 012007.
- 42. Kibsgaard, J.; Chorkendorff, I., Considerations for the Scaling-up of Water Splitting Catalysts. *Nat. Energy* **2019**, 4, 430-433.
- 43. Anantharaj, S.; Noda, S.; Driess, M.; Menezes, P. W., The Pitfalls of Using Potentiodynamic Polarization Curves for Tafel Analysis in Electrocatalytic Water Splitting. *ACS Energy Lett.* **2021**, 6, 1607-1611.
- 44. Chen, W.-T.; Hsu, C.-W.; Lee, J.-F.; Pao, C.-W.; Hsu, I.-J., Theoretical Analysis of Fe K-Edge Xanes on Iron Pentacarbonyl. *ACS Omega* **2020**, 5, 4991-5000.
- 45. Randall, C. R.; Shu, L.; Chiou, Y.-M.; Hagen, K. S.; Ito, M.; Kitajima, N.; Lachicotte, R. J.; Zang, Y.; Que, L., X-Ray Absorption Pre-Edge Studies of High-Spin Iron(Ii) Complexes. *Inorg. Chem.* 1995, 34, 1036-1039.

- 46. Wasinger, E. C.; de Groot, F. M. F.; Hedman, B.; Hodgson, K. O.; Solomon, E. I., L-Edge X-Ray Absorption Spectroscopy of Non-Heme Iron Sites: Experimental Determination of Differential Orbital Covalency. *J. Am. Chem. Soc.* **2003**, 125, 12894-12906.
- 47. Wang, D.; Zhou, J.; Hu, Y.; Yang, J.; Han, N.; Li, Y.; Sham, T.-K., In Situ X-Ray Absorption near-Edge Structure Study of Advanced Nife(Oh)X Electrocatalyst on Carbon Paper for Water Oxidation. *J. Phys. Chem. C* **2015**, 119, 19573-19583.
- 48. Yuge, R.; Kuroshima, S.; Toda, A.; Miyazaki, T.; Tabuchi, M.; Doumae, K.; Shibuya, H.; Tamura, N., Structural and Electrochemical Properties of Iron- and Nickel-Substituted Li₂mno₃ Cathodes in Charged and Discharged States. *J. Power Sources* **2017**, 365, 117-125.
- 49. Landon, J.; Demeter, E.; Inoglu, N.; Keturakis, C.; Wachs, I. E.; Vasic, R.; Frenkel, A. I.; Kitchin, J. R., Spectroscopic Characterization of Mixed Fe–Ni Oxide Electrocatalysts for the Oxygen Evolution Reaction in Alkaline Electrolytes. *ACS Catal.* **2012**, 2, 1793-1801.
- 50. Kim, S.; Tryk, D. A.; Antonio, M. R.; Carr, R.; Scherson, D., In Situ X-Ray Absorption Fine Structure Studies of Foreign Metal Ions in Nickel Hydrous Oxide Electrodes in Alkaline Electrolytes. *J. Phys. Chem.* **1994**, 98, 10269-10276.
- 51. Bates, M. K.; Jia, Q.; Doan, H.; Liang, W.; Mukerjee, S., Charge-Transfer Effects in Ni–Fe and Ni–Fe–Co Mixed-Metal Oxides for the Alkaline Oxygen Evolution Reaction. *ACS Catal.* **2016**, 6, 155-161.
- 52. Mansour, A.; Melendres, C.; Pankuch, M.; Brizzolara, R., X-Ray Absorption Fine Structure Spectra and the Oxidation State of Nickel in Some of Its Oxycompounds. *J. Electrochem. Soc.* **1994**, 141, L69.

- 53. Balasubramanian, M.; Melendres, C.; Mini, S., X-Ray Absorption Spectroscopy Studies of the Local Atomic and Electronic Structure of Iron Incorporated into Electrodeposited Hydrous Nickel Oxide Films. *J. Phys. Chem. B* **2000**, 104, 4300-4306.
- 54. McBreen, J.; O'Grady, W.; Tourillon, G.; Dartyge, E.; Fontaine, A.; Pandya, K., In Situ Time-Resolved X-Ray Absorption near Edge Structure Study of the Nickel Oxide Electrode. *J. Phys. Chem.* **1989**, 93, 6308-6311.
- 55. Jing, P.; Liu, M.; Pu, Y.; Cui, Y.; Wang, Z.; Wang, J.; Liu, Q., Dependence of Phase Configurations, Microstructures and Magnetic Properties of Iron-Nickel (Fe-Ni) Alloy Nanoribbons on Deoxidization Temperature in Hydrogen. *Sci. Rep.* **2016**, 6, 37701.
- 56. Shabashov, V. A.; Lapina, T. M.; Pilyugin, V. P., Isothermal Bcc↔Fcc Phase

 Transformations in Fe-Ni Alloys with a Submicrograin Structure. *Nanostruct. Mater.* **1997**, 9, 677-680.
- 57. Pirngruber, G. D.; Grunwaldt, J.-D.; van Bokhoven, J. A.; Kalytta, A.; Reller, A.; Safonova, O. V.; Glatzel, P., On the Presence of Fe(Iv) in Fe-Zsm-5 and Fesro3-Xunequivocal Detection of the 3d4 Spin System by Resonant Inelastic X-Ray Scattering. *J. Phys. Chem. B* **2006**, 110, 18104-18107.
- 58. Haas, O.; Vogt, U. F.; Soltmann, C.; Braun, A.; Yoon, W. S.; Yang, X. Q.; Graule, T., The Fe K-Edge X-Ray Absorption Characteristics of La1–Xsrxfeo3–Δ Prepared by Solid State Reaction. *Mater. Res. Bull.* **2009**, 44, 1397-1404.
- 59. Kuzmin, A.; Chaboy, J., Exafs and Xanes Analysis of Oxides at the Nanoscale. *IUCrJ* **2014**, 1, 571-589.

- 60. Jiang, J.; Sun, F.; Zhou, S.; Hu, W.; Zhang, H.; Dong, J.; Jiang, Z.; Zhao, J.; Li, J.; Yan, W.; Wang, M., Atomic-Level Insight into Super-Efficient Electrocatalytic Oxygen Evolution on Iron and Vanadium Co-Doped Nickel (Oxy)Hydroxide. *Nat. Commun.* **2018**, 9, 2885.
- 61. Wang, L.; Wen, Y.; Ji, Y.; Cao, H.; Li, S.; He, S.; Bai, H.; Liu, G.; Zhang, L.; Bao, H.; Wang, J.; Li, Y.; Zhang, B.; Peng, H., The 3d–5d Orbital Repulsion of Transition Metals in Oxyhydroxide Catalysts Facilitates Water Oxidation. *J. Mater. Chem. A* **2019**, 7, 14455-14461.
- 62. Coduri, M.; Masala, P.; Bianco, L. D.; Spizzo, F.; Ceresoli, D.; Castellano, C.; Cappelli, S.; Oliva, C.; Checchia, S.; Allieta, M., Local Structure and Magnetism of Fe₂o₃ Maghemite Nanocrystals: The Role of Crystal Dimension. *Nanomater.* **2020**, 10, 867.
- 63. Harada, M.; Kuwa, M.; Sato, R.; Teranishi, T.; Takahashi, M.; Maenosono, S., Cation Distribution in Monodispersed Mfe₂o₄ (M = Mn, Fe, Co, Ni, and Zn) Nanoparticles Investigated by X-Ray Absorption Fine Structure Spectroscopy: Implications for Magnetic Data Storage, Catalysts, Sensors, and Ferrofluids. *ACS Appl. Nano Mater.* **2020**, 3, 8389-8402.
- 64. Fdez-Gubieda, M. L.; García-Prieto, A.; Alonso, J.; Meneghini, C. X-Ray Absorption Fine Structure Spectroscopy in Fe Oxides and Oxyhydroxides. In *Iron Oxides*, 2016; pp 397-422.
- 65. Okudera, H.; Yoshiasa, A.; Murai, K.-i.; Okube, M.; Takeda, T.; Kikkawa, S., Local Structure of Magnetite and Maghemite and Chemical Shift in Fe K-Edge Xanes. *J. Mineral. Petrol. Sci.* **2012**, 107, 127-132.
- 66. Enman, L. J.; Stevens, M. B.; Dahan, M. H.; Nellist, M. R.; Toroker, M. C.; Boettcher, S. W., Operando X-Ray Absorption Spectroscopy Shows Iron Oxidation Is Concurrent with

Oxygen Evolution in Cobalt–Iron (Oxy)Hydroxide Electrocatalysts. *Angew. Chemie Int. Ed.* **2018**, 130, 13022-13026.

- 67. Ewing, F. J., The Crystal Structure of Lepidocrocite. J. Chem. Phys. 1935, 3, 420-424.
- 68. Szytuła, A.; Burewicz, A.; Dimitrijević, Ž.; Kraśnicki, S.; Rżany, H.; Todorović, J.; Wanic, A.; Wolski, W., Neutron Diffraction Studies of A-Feooh. *Phys. Status Solidi B* **1968**, 26, 429-434.
- 69. Hall, D. S.; Lockwood, D. J.; Bock, C.; MacDougall, B. R., Nickel Hydroxides and Related Materials: A Review of Their Structures, Synthesis and Properties. *Proc. Math. Phys. Eng. Sci.* **2015**, 471, 20140792-20140792.
- 70. McBreen, J.; O'Grady, W. E.; Pandya, K. I.; Hoffman, R. W.; Sayers, D. E., Exafs Study of the Nickel Oxide Electrode. *Langmuir* **1987**, 3, 428-433.
- 71. Németh, Z.; Bajnóczi, É. G.; Csilla, B.; Vankó, G., Laboratory Exafs Determined Structure of the Stable Complexes in the Ternary Ni(Ii)–Edta–Cn System. *Phys. Chem. Chem. Phys.* **2019**, 21, 9239-9245.
- 72. Pandya, K. I.; O'Grady, W. E.; Corrigan, D. A.; McBreen, J.; Hoffman, R. W., Extended X-Ray Absorption Fine Structure Investigations of Nickel Hydroxides. *J. Phys. Chem. C* **1990**, 94, 21-26.

TOC Graphic: For Table of Contents Only

